International Journal of Greenhouse Gas Control 133 (2024) 104105

Contents lists available at ScienceDirect

International Journal of Greenhouse Gas Control

journal homepage: www.elsevier.com/locate/ijggc

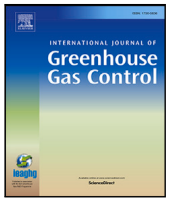

Modelling geological CO_2 leakage: Integrating fracture permeability and fault zone outcrop analysis

Roberto Emanuele Rizzo [a,b,c,*], Nathaniel Forbes Inskip [c], Hossein Fazeli [c], Peter Betlem [d,e], Kevin Bisdom [f], Niko Kampman [g], Jeroen Snippe [f], Kim Senger [d], Florian Doster [c], Andreas Busch [c]

[a] Department of Earth Sciences, University of Florence, Via Giorgio La Pira 4, Florence, 50121, Italy
[b] School of Geosciences, University of Edinburgh, The King's Buildings, James Hutton Road, Edinburgh, EH9 3FE, Scotland, United Kingdom
[c] The Lyell Centre for Earth and Marine Science and Technology, Edinburgh, EH14 4AS, Scotland, United Kingdom
[d] Department of Arctic Geology, The University Centre in Svalbard, Longyearbyen, N-9171, Svalbard, Norway
[e] Department of Geosciences, University of Oslo, Sem Sælands vei 1, Oslo, N-0371, Norway
[f] Shell Global Solutions International B.V., Grasweg 31, Amsterdam, 1031 HW, The Netherlands
[g] Nuclear Waste Services, Building 329, West, Harwell Science & Innovation Campus, Thomson Ave, Didcot, OX11 OGD, England, United Kingdom

ARTICLE INFO

Dataset link: FracPaQ, MRST, SVALBOX, Svalbox Digital Model Database

Keywords:
Fracture permeability
Fault damage zone analysis
Outcrop studies
Geological carbon capture and storage
Permeability modelling

ABSTRACT

Geological carbon capture and storage (CCS) is a critical technology for mitigating greenhouse gas emissions, but the risk of leakage remains a significant concern. Fault and fracture networks across sealing intervals are potential pathways for CO_2 to escape from storage reservoirs, necessitating accurate assessment of their permeability and connectivity. Our study presents an integrated approach for modelling geological leakage in fault zones, combining single fracture stress-permeability laboratory measurements with detailed fracture outcrop data to simulate in-situ conditions for carbon storage. We studied caprock sequences cut by a normal fault in the Konusdalen West area (Svalbard, Norway), a regional seal for the reservoir of the Longyearbyen CO_2 Laboratory, and an analogue to Barents and North seas caprock formations. Digitising the outcropping fracture network, we explored the variations in fracture size distribution and their connectivity in different portions of the fault zone. These parameters are fundamental to establish if the fracture network provides permeable pathways. Integrating outcrop analysis with laboratory measurements allows us to create coupled hydromechanical models of the natural fracture network and to evaluate their upscaled permeability. We found that fracture network geometries vary across the fault zone, resulting in different upscaled permeability models, thus highlighting the importance of including detailed fracture network information into permeability simulations. Our study provides a framework for incorporating fracture permeability measurements and outcrop analysis into the modelling of geological leakage in fault zones, which can inform the design and operation of CCS projects and help mitigate the risks associated with geological storage of CO_2.

1. Introduction

There is a global need to increase our ambitions to reduce net greenhouse gas emissions to mitigate climate change (e.g., European Commission's Climate Target Plan 2030) and Carbon Capture and Storage (CCS) has the potential to contribute significantly to low-carbon energy system transitions (IIPCC, 2022). Resource extraction from the subsurface (i.e., hydrocarbons, geothermal energy, water) has demonstrated that subsurface activities are prone to uncertainties and, consequently, risks. Uncertainty and risk management is therefore an integral aspect of industrial activities involving subsurface operations. CO_2 leakage through the caprock is one of the main risks related to geological CO_2 storage projects, whereby fluid migration may result in CO_2 reaching (and contaminating) overlying aquifers or the surface. Although effective caprocks are characterised by undisturbed, low permeability ($<10^{-19}m^2$), thick, and laterally extensive formations (Amann-Hildenbrand et al., 2013; Busch and Amann-Hildenbrand, 2013), the presence of faults and fractures represents a significant threat to caprock integrity (Fig. 1). Faults and their associated fracture

* Corresponding author at: Department of Earth Sciences, University of Florence, Via Giorgio La Pira 4, Florence, 50121, Italy.
E-mail addresses: robertoemanuele.rizzo@unifi.it, robertoemanuele.rizzo@gmail.com (R.E. Rizzo).

https://doi.org/10.1016/j.ijggc.2024.104105
Received 2 August 2023; Received in revised form 30 January 2024; Accepted 26 February 2024
Available online 6 March 2024

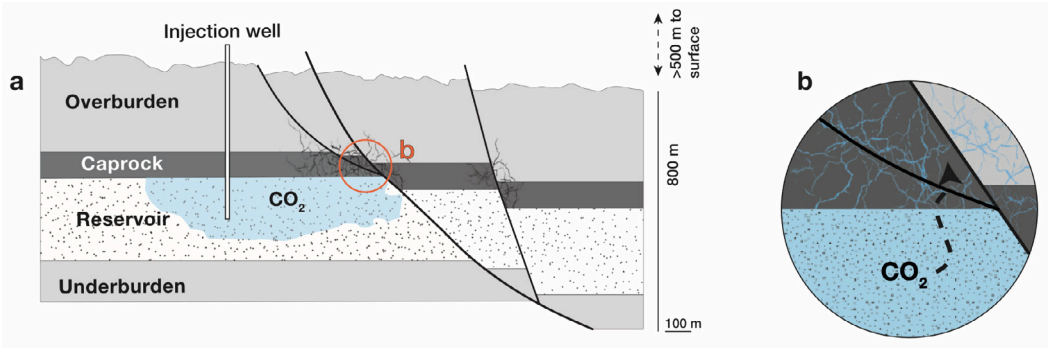

Fig. 1. Sketch showing a cross-section of the subsurface, with a fault cutting through layered formations. The fault is shown as a black line with the surrounding fractured damage zone depicted in lighter grey pattern (a). CO_2 migration is illustrated in the closer caption (b) by arrows moving through the fault and fracture networks.

networks can serve as conduits through which fluids can escape (Bond et al., 2013). Thus, understanding the distribution and architecture of these geological features, as well as their transport and geomechanical properties, is critical for accurately assessing storage safety.

Faults are complex geological features consisting of a well-localised fault core surrounded by a fractured damage zone (Faulkner et al., 2011; Phillips et al., 2020). The damage zone can extend tens of metres away from the fault core and is characterised by a network of fractures (Faulkner et al., 2011). Observations from outcrop analogues and laboratory studies found that in mudrocks, the pathway of migrating fluids is often structurally controlled by faults and the associated fracture networks (Dewhurst et al., 1999; Aiello, 2005; Palladino et al., 2020). While fault cores are relatively low-permeability zones, the fracture-dominated damage zones can exhibit permeabilities up to six orders of magnitude greater than the fault core, making them highly conductive regions (Caine et al., 1996). However, the sub-seismic scale of fractures means that their presence, properties, and ability to form larger scale connected networks are major uncertainties in CO_2 storage operations. To address these uncertainties, it is essential to use outcrop data as a link between data collected at core scale and those collected at reservoir scale. This approach can provide valuable insights into the distribution and architecture of fault and fracture networks and help reduce uncertainty in CO2 storage operations. The viability of current and future CCS projects therefore relies not only on the efficiency of fluid transport within geological formations, but also on the ability of caprock formations to effectively contain fluids over millennia timescales.

Given the potential risks associated with CO_2 leakage through fault damage zones in caprocks, de-risking CCS projects requires an improved understanding of how these geological features can contribute to fluid migration. In this context, we present a new workflow for assessing leakage risks by integrating outcrop-derived fracture data, laboratory measurements of single fracture permeability, and numerical modelling. Our approach involves three main objectives: First, we examine how fracture networks and their geometrical relationships (i.e., topology) can influence fluid flow pathways. To accomplish this, we digitise a dense fracture network associated with a large normal fault cutting the Agardhfjellet Formation shale exposed in the Konusdalen West, Deltaneset area in Svalbard (Norway), and analyse the digitised fractures using the MATLAB toolbox FracPaQ (Healy et al., 2017). Our results show that the fracture networks differ in different portions of the fault damage zone both in terms of fracture attributes (length and orientation), and in terms of spatial/topological organisation with reference to the connectivity of the networks. Secondly, we compare the effects of different fracture network geometrical properties in upscaled stress-permeability models. This involves the integration of outcrop-derived fracture data with laboratory-derived stress-dependent fracture permeability measurements. Laboratory petrophysical measurements provide critical information on how stress changes can affect both intrinsic and fracture permeability, albeit on a small scale (Van Stappen et al., 2014, 2018). By integrating laboratory, outcrop, and numerical methods, we can construct meaningful and realistic upscaled permeability models based on coupled hydro-mechanical simulations. Finally, our study aims to highlight the discrepancies and insights gained from comparing different approaches to calculate permeability for fractured systems: a hydromechanical numerical simulation against two analytical bulk permeability estimations derived from solely geometrical and topological data. While the individual methodologies employed are not new, our contribution lies in the innovative integration of these approaches. This comparative analysis forms the essence of our workflow, designed to enhance our understanding of how fault damage zones may contribute to CO_2 migration through caprocks in CCS projects.

This paper, therefore, serves both as a site-specific first-order investigation and as a methodological exercise with implications for similar geological settings in CCS projects. Our findings underscore the need for a comprehensive approach that considers both the geometrical and mechanical aspects of fracture networks, thus contributing to the de-risking of CCS projects.

2. Konusdalen west site overview

The Svalbard archipelago is part of the emerged, uplifted northwest Barents Shelf (Olaussen et al., 2024). The rocks cropping out on the islands have recorded a series of deformation events starting from the Caledonian Orogeny to the establishment of a Cenozoic transform plate margin Braathen et al. (2012), Mulrooney et al. (2018). In the late Cretaceous, a dextral transform zone, known as the De Geer Zone, developed between Greenland (to the West) and Svalbard (to the East). The consequent oblique transpression led to the development of the West Spitsbergen Fold-and-Thrust Belt (WSFTB) and the Paleogene Central Spitsbergen Basin (CSB), a foredeep to wedge-top basin filled with mixed continental and marine clastics (Ogata et al., 2014 and references therein). The WSFTB is characterised by a western thick-skinned province where structures are basement-involved, and an eastern thin-skinned fold-and-thrust belt with three distinct detachment levels (i.e., décollements) along weak evaporite and shale intervals, two of which stratigraphically bound the studied site (Ogata et al., 2014; Mulrooney et al., 2018). In addition, smaller-scale extensional faults that offset the storage-seal sequences are found in this area and have been related to differential tectonic loading during the evolution of the WSFTB (Ogata et al., 2014; Mulrooney et al., 2018). Svalbard has gone through several phases of deglaciation causing isostatic rebound and decompaction. In the Cenozoic, erosion and especially glacial erosion was an active process. This has led to approximately 3.5 km of uplift in central Spitsbergen (Bohloli et al., 2014). The strata present shows loading mechanisms, and later the unloading and erosion of the overburden displayed as unloading joints, probably reactivated during the deglaciation and decompaction (Ogata et al., 2014).

The Longyearbyen CO_2 Laboratory project is an onshore, pilot-scale site for geological CO_2-sequestration at depths between 700 m and 1000 m on central Spitsbergen, Svalbard (Olaussen et al., 2024; Braathen et al., 2012 and references therein). In this project the targeted storage unit is an aquifer made up of a siliciclastic succession belonging to the Upper Triassic – Middle Jurassic Kapp Toscana Group (Fig. 2). It includes the De Geerdalen Formation – a 270 m-thick heterolithic units – with and elements of the overlying Wilhelmøya Subgroup – a 20 m- thick condensed siliciclastic unit. These units are overlain by the Middle Jurassic—Lower Cretaceous Agardhfjellet and Rurikfjellet, predominantly shaly, formations, which act as the targeted caprock (Fig. 2). On central Spitsbergen these formations are measured to be more than 400 m thick (Ogata et al., 2014; Mulrooney et al., 2018). As part of the Longyearbyen CO_2 project (Olaussen et al., 2024 and references therein), water-injection tests were conducted to measure the reservoir injectivity. Approximately 1500 m^3 of water were injected through the DH7 A borehole in September 2012, at a near stable rate of $\approx\sim$ 460 m^3/day (Senger et al., 2015; Birchall et al., 2020). These tests confirmed good injectivity and flow capacity of 39 mD·m, but also highlighted that the target reservoir is compartmentalised as two wells, which are 94 m apart, were not in direct communication and thus, lateral flow barriers must be present (Mulrooney et al., 2018). Detailed field mapping of the outcropping reservoir/caprock at Deltaneset 15 km northeast of the Longyearbyen CO_2 Laboratory injection site reveals a series of potential seal bypass systems that include sedimentary intrusions (Ogata et al., 2023) and normal faults that are equally likely to contribute to reservoir compartmentalisation (Ogata et al., 2014; Mulrooney et al., 2018; Betlem et al., 2024, 2023; Ogata et al., 2023).

Our studied site is located in the Deltaneset area (Nordenskiold Land) on the northeast (NE) margin of the CBS (Fig. 2), exposing the shale-dominated succession belonging to the Middle Jurassic to Early Cretaceous Agardhfjellet Formation and the Early Cretaceous Rurikfjellet Formation in Konusdalen and Konusdalen West (Mulrooney et al., 2018; Betlem et al., 2024, 2023; Ogata et al., 2023). The shale-rich sequences of the Agardhfjellet Formation are the outcrop analogues of the lower part of the regional caprock. A regional décollement ("upper décollement", Fig. 2c) is interpreted to sit along the boundary of the two Formations (Koevoets et al., 2018). Our studied area (red box in Fig. 2c) exposes a system of mesoscale normal faults characterised by displacement of up to a few tens of metres and striking roughly NE-SW; antithetic faults are also present. These extensional structures are situated down-section from the regional contractional features: Ogata et al. (2014) interpreted this normal fault system as a result of differential loading during the formation of the Paleogene WSFTB. Betlem et al. (2024) provide a more extensive description of the Konusdalen West, including a stratigraphic correlation with the Longyearbyen CO2 Laboratory boreholes.

3. Methods

3.1. Outcrop data acquisition and analysis

For this study, we reprocessed digital outcrop model (DOM) data available through the Svalbox project and the Svalbox Digital Model Database (Betlem and Team, 2021; Betlem et al., 2023). The sub-set of data were originally acquired using a DJI Mavic 2 Pro Unmanned Aerial Vehicle (UAV, i.e., drone) and cover a vertical section of the Konusdalen West Valley, which has a near N–S-trend (location shown in Fig. 2). Processing implemented the Structure for Motion (SfM) photogrammetry technique and the Agisoft Metashape software suite (1.6.3 build 10732) to produce a high-resolution DOM and an orthomosaic of the area of interest (Fig. 3). Images were taken from $\approx$ 60 m above the ground, resulting in an excellent ground sampling distance and ground pixel resolution of 1.27 cm/px for the resulting 2D orthomosaic. The pixel resolution resembles the imaging limit of the data, and subpixel features may not be confidently interpreted especially when they are less distinctive or opaque transitions (e.g., coarsening trends). Distinctive features (such as fractures) are likely to dominate the pixel values, increasing interpretation confidence. However, similar to fault tracing in seismic, subpixel features may be inferred from small-scale offsets and terminations or can be implicitly derived from trends that span distances that are several times that of the pixel dimension (Betlem et al., 2023). The supplementary materials section contains a processing report that details the implemented processing parameters, following community best-practices (Betlem et al., 2023; Over et al., 2021).

To obtain information on fault and fracture attributes (i.e., length, orientation trend) and on their mutual geometrical/topological relationships (i.e., density, connectivity) we used FracPaQ, a freely available MATLAB software (Healy et al., 2017). This software comprises a suite of tools that allow to consistently quantify fracture patterns and their variations in 2D. Fracture maps were produced by manually tracing all the fractures visible on the extracted orthomosaics of the acquired outcrop virtual models in the Konusdalen West area. Although time-consuming and potentially susceptible to some subjectivity (Andrews et al., 2019; Weismuller et al., 2020), manual tracing allows a user to discern and identify specific features (e.g., discriminating fractures from artefacts) which can be difficult to distinguish by an automated analysis (Griffiths et al., 2017; Rizzo et al., 2018). From these inputs FracPaQ generates several diagrams (e.g., colour-coded maps for trace and segment fracture lengths) and plots (e.g., orientation distribution, histogram of lengths) which help to visualise area distributions of fracture attributes in a rock mass.

We used a combination of Maximum-Likelihood Estimation (MLE) and Kolmogorov-Smirnoff (KS) statistical tests to determine the most suitable distribution for the measured fracture length data (Clauset et al., 2009; Rizzo et al., 2017). MLE is employed to estimate the parameters of statistical models, specifically to identify which distribution (power-law, exponential, or log-normal) best represents the observed fracture lengths (Bonnet et al., 2001; Gillespie et al., 1993; Zeeb et al., 2013; Dichiarante et al., 2020). This approach involves finding the most likely parameters for our selected statistical models that fit the observed data. In a MLE plot (see Fig. 5C and Fig. 6C), each point represents a fracture length value, and the y-axis signifies the probability of encountering another fracture of equal or greater length. This analysis is integral to examining the size distribution of the fracture networks, thereby providing essential insights into the characteristics and behaviour of the studied fracture systems. Consequently, the statistical analysis of fracture attributes from outcrop analogues offers valuable and robust geological information for building simulation models (Mäkel, 2007; Dichiarante et al., 2020).

We derived a distribution of fracture density – here defined as the number of fractures per unit area (in m^2) – over the analysed fracture networks by applying the circular scan window method introduced by Mauldon et al. (2001). The method is implemented in the FracPaQ software and consists in superimposing a circle of known diameter over the fracture network and counting the number fractures terminating within the circle (Rohrbaugh et al., 2002; Zeeb et al., 2013). Full expression of the formula used for this measure can be found in Appendix A to this paper.

Fracture network connectivity is a further fundamental measure needed to assess the ability of fracture networks to sustain fluid flow. Fracture connectivity values derived from topological measurements of fracture intersections, labelled as I, Y, X nodes (Manzocchi, 2002). Nodes are classified as "I" for isolated ends of fracture traces; "Y" for branching, splays or abutments and "X" for cross-cutting intersection. The portion of a fracture connected or terminating at a node is defined as a "branch" (Sanderson and Nixon, 2015). The FracPaQ software draws a ternary plot of fracture connectivity with the three vertices of the triangle denoting I, Y, X nodes in the fracture network. The relative proportions of these nodes are then calculated with respect to the total number of intersections found. Well-connected networks will plot towards the lower Y–X tie of the diagram, whereas less

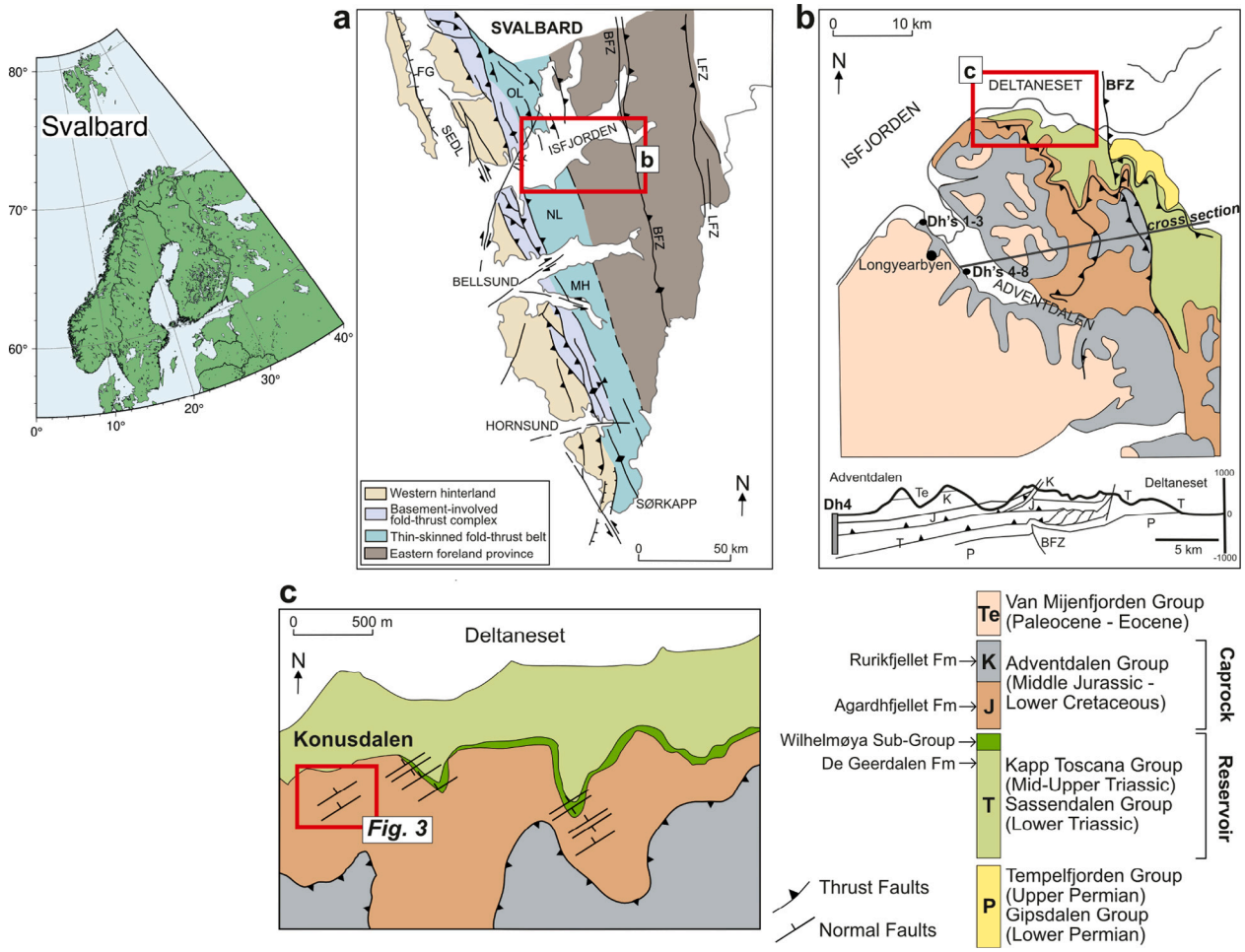

Fig. 2. Geological overview of the study area. (a) Geotectonic domains of south- central Spitsbergen area [modified after Braathen et al. 2012]. (b) Geological map of Central Spitsbergen around Longyearbyen, with a WSW–ENE structural cross section. Note the location of the city of Longyearbyen and the drilling sites of wells Dh1-Dh8 for the Longyearbyen CO_2 Laboratory project on the map [modified after (Braathen et al., 2012). (c) Location of east-facing outcrop for which virtual outcrop model was generated [modified after Lubrano-Lavadera et al. 2018]. Abbreviations: BFZ — Billefjorden Fault Zone, FG — Forlandsundet graben, LFZ — Lomfjorden Fault Zone, NL — Nordenskiold Land, MH — Midterhuken, OL — Oscar II land, SEDL — Svartfjell–Eidembukta–Daumannsodden lineament, Cp — Carboniferous–Permian, Tr — Triassic, JC — Jurassic–Cretaceous.

connected networks will plot towards the I apex. Manzocchi (2002) and, subsequently, Sanderson and co-workers (Sanderson and Nixon, 2015, 2018; Sanderson et al., 2019) defined a number of dimensionless parameters able to quantitatively evaluate the degree of connectivity of a fracture network, which in turn can be used to assess the percolation path of fluids (e.g., water or CO_2) through the analysed rock mass (described in full in Appendix B).

The information obtained from the outcrop analysis of a fracture network can be directly used to estimate the fracture network permeability. These analytical methods use either geometrical (i.e., fracture size, orientation, and density) or topological (i.e., fracture connectivity) information.

3.2. Laboratory experiments

3.2.1. Sample material

Unfortunately, due to Covid-19 related constraints, we were unable to obtain sample material from the Rurikfjellet shale for this study. Consequently, we selected an analogue material from the Carmel Formation that exhibited similar mineralogy and mechanical properties, which are crucial for understanding fracture closure under stress (Snippe et al., 2022). This choice, while a compromise, allowed us to develop and validate a workflow that can be applied to various lithologies, including the local Rurikfjellet shale, once samples become available. This adaptability of our workflow underscores its value in broader geomechanical contexts.

Although literature data are available (van Noort and Yarushina, 2018) for the upper caprock Rurikfjellet Formation, we deemed the existing Rurikfjellet shale data inappropriate to use in our work because the fractures in the samples seal due to compaction under stress, as reported by the authors. This sealing, whether caused solely by compaction or any process involving water, results in permeability values representing matrix permeability, hence not suitable to use for in our study . Thus, we conducted permeability measurements on analogue sample material of Carmel claystone containing a fracture, for use in this study. Samples of the Carmel claystone (core plugs 2,54 cm in diameter and 5,08 cm in length) were taken from the wellbore core retrieved as part of the scientific drilling campaign near Green River in Utah, USA (Kampman et al., 2014).

The Carmel claystone, a quartz-rich mudrock, serves as a caprock for natural CO_2 accumulations in the Paradox Basin, Utah, USA. Its mineralogy resembles a shale, with the studied sample composed of 44% quartz, 29% illite/muscovite, 15% alkali-feldspar, 6% smectite, and trace amounts of other minerals (each constituting less than 4%). Which compares reasonably well to the composition of the quartz rich Rurikfjellet formation as reported by Van Noort and Yarushina [2019] of 55%–60% quartz, 20%–25% illite with minor interlayered smectite and chlorite, with other minor phases including kaolinite, plagioclase and pyrite. Mineralogy has a strong control on the mechanical

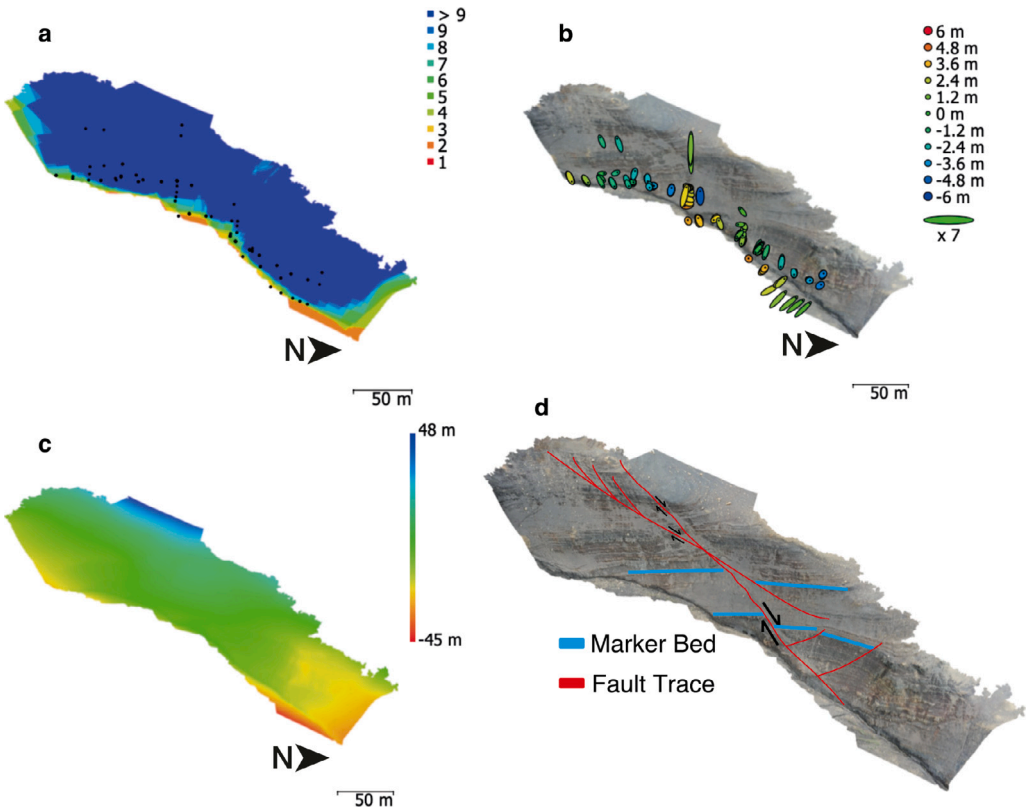

Fig. 3. UAV survey data outputs for the vertical section in the Konusdalen West outcrop. (a) UAV camera locations and image overlap; colours indicate image overlap. (b) UAV camera locations and error estimates, vertical (Z) error is represented by ellipse colours; horizontal (X, Y) errors are represented by ellipse shape. (c) Reconstructed digital elevation model. (d) High-resolution orthomosaic reconstruction. More details on the digital model outcrop model can be found in Supplementary Materials.

properties of a rock, such as Young's modulus (Rybacki et al., 2015; Askaripour et al., 2022; Abu-Mahfouz et al., 2023). When confining pressure is applied to a fractured sample (or to a fracture in the subsurface), the fracture opening decreases but a non-zero aperture can be maintained by the presence of asperities on the fracture surface that prevent the full closing of a fracture (Phillips et al., 2020). The asperities' ability to keep the fracture open under stress depends in part on the Young's modulus of the material (Snippe et al., 2022). The Carmel claystone's Young's modulus ranges between 12.5 and 25.1 GPa (O'Rourke et al., 1986). By comparison, the Young's modulus of the Rurikfjellet shale ranges from 5.17 to 13.20 GPa, while the typical range for the Agardhfjellet Formation is between 7.47 and 10.7 GPa, though it can reach as high as 44.34 GPa (Abbas, 2015; Bohloli et al., 2014).

3.2.2. Laboratory permeability measurements

We measured the permeability of a Carmel claystone sample using the steady-state method, with nitrogen as permeating fluid and at a constant temperature of 25 °C. The raw data used for this analysis has been published previously (Phillips et al., 2020), providing permeability values on the plug scale. Hydromechanical models, however, require the relationship between fracture aperture and effective stress as input. Consequently, to convert the measured fracture permeability data into fracture aperture values, we use the analytical relationship described by Zhang (2011, 2013) as follows (see also Phillips et al. (2020) and Kubeyev et al. (2022) for further details):

$$k_{bulk} = k_{matrix} + k_{fracture} + \frac{F}{12}(b - b_c)^3 \quad (1)$$

where k_{bulk}, k_{matrix} and $k_{fracture}$ are sample, matrix and fracture permeabilities, respectively, b is the fracture aperture, b_c is the critical aperture (i.e., the highest aperture that critically connects the inflow and out-flow sides of the fracture), and F is a geometric parameter related to sample dimensions by:

$$F = 4/\pi d \quad (2)$$

where d is the diameter of the sample. Fracture aperture, b, is then calculated by:

$$b = b_m - \Delta b \quad (3)$$

where b_m, the initial unstressed aperture, and Δb, the fracture closure, are approximated by:

$$b = b_m(1 - e^{\alpha\sigma^{\beta}{}_{eff}}) \quad (4)$$

where $alpha$ and $beta$ are constants. If k_{matrix}, d, and $sigma_{eff}$ are known, then the values of b_c, b_m, $alpha$ and β can be deduced through a curve fitting exercise tuning the fitting parameters to adjust the permeability model to the measured sample permeability. The aperture/permeability model allows us to evaluate the fracture aperture and permeability based on the contact stress. This information is then used as inputs for the flow simulations allowing us to retrieve a flow field for the whole fracture network as a function of a fluid pressure gradient (March et al., 2020).

3.3. Permeability estimation and modelling of fault and fracture networks

3.3.1. Analytical permeability estimation for fault and fracture networks

A common analytical method to estimate permeability of faulted and fractured rock masses is based on the combination of the cubic law and the crack-tensor formulation as expressed by Suzuki et al. (1998), Brown and Bruhn (1998), and Oda (1985). The crack tensor incorporates information about fracture size (length and aperture), orientation and spatial densities. FracPaQ allows us to derive this

information using 2D fracture maps. The crack tensor is calculated accordingly to:

$$P_{ij} = \frac{\pi}{4V} \sum r^2 t^3 n_i n_j = \frac{\pi}{4} \rho \langle r^2 \rangle \langle t^3 \rangle N_{ij} \quad (5)$$

where ρ is the fracture density, $\langle r^2 \rangle$ is the mean of the squared fracture length, $\langle t^3 \rangle$ is the mean of the cubed aperture, and N_{ij} is the fracture orientation matrix. Thus, the permeability can be computed as:

$$k_{ij} = \frac{\lambda}{12}(P_{kk}\delta_{ij} - P_{ij}) \quad (6)$$

here λ is a factor that varies between 0 and 1, and δ is the Kronecker delta.

In the FracPaQ implementation the aperture term, t, is derived from the length distribution, assuming that fracture aperture increases with its length. This scaled aperture (t) is obtained according to a power-law, $t = ar^b$ (Vermilye and Scholz, 1995), where aperture t is a function of segment length r, a is a constant factor and b is a power law exponent ≥ 1.

A second analytical method to estimate permeability is based on the work of Sævik and Nixon (2017) and uses a simple formulation based on the relative proportion of the I-Y-X nodes. It comprises an expression for the upper bound for the permeability assuming all fractures are fully connected:

$$k_{eff} = \frac{f}{A} \sum_{i=1}^{N} T_i \; L_i \theta_i \quad (7)$$

in this equation f indicates the hydraulic connectivity, which is a measure of how well connected the fractures are in the network. A is the total area of the fractured rock, N is the total number of fractures and T, L and θ are the transmissivity factor (aperture x permeability), the length and the angle from the vertical of the ith fracture, respectively. In Sævik and Nixon (2017) formulation, the f factor is analytically estimated from fracture node connectivity as:

$$f = max(0, \frac{2.94 \cdot (4n_X + 2n_Y)}{4n_X + 2n_Y + n_I} - 2.13) \quad (8)$$

where n_X, n_Y and n_I are the number of X-nodes, Y-nodes, and I-nodes, respectively.

The two described analytical methods have the limitation of not explicitly taking into account stress conditions when resolving permeability estimates for a fracture network. Nonetheless, they have the advantage of being fast, if compared to numerical simulations, thus making them widely used approaches (Niven and Deutsch, 2009). In this work, we will compare the results obtained using the analytical methods against stress-permeability numerical models, as the geometrical approaches can serve as a first approximation for numerical simulations.

3.3.2. Numerical permeability calculations for fault and fracture networks

In this study, we follow the method described in March et al. (2020) to calculate upscaled permeability under various stress conditions for a digitised 2D field fracture network. The 2D digitised fault and fracture network is discretised using a triangular finite element mesh that conforms to the fracture. This workflow involves applying stresses to an augmented rock mass surrounding the meshed fracture network (i.e., a buffer around the fractures to avoid boundary effects), with stress boundary conditions applied to the 2D networks. A buffer zone is considered around the fracture networks to mitigate boundary effects.

Fractures are modelled as material discontinuities that lie within the domain, thus allowing to compute contact stresses within individual fractures using a simplified contact mechanics algorithm in response to the applied stress. These contact stresses, representing the normal stress experienced by fracture walls, are used to determine the aperture of each fracture segment. Fracture apertures are calculated using the contact stresses and the experimental model (Eq. (3)), which expresses the stress-aperture relationship for a single fracture. This experimental data enables the reproduction of accurate single-fracture stress-aperture behaviour for the studied rock type.

The flow model solves for the pressure gradient (in either the vertical or the horizontal direction) through the digitised fracture network, assuming single-phase flow with an impermeable matrix (since the matrix of the caprock is considered impermeable). The effective permeability is then calculated from the pressure gradient using Darcy's equation. This workflow is implemented in the MATLAB Reservoir Simulation Toolbox (MRST) (Lie, 2019), chosen for its three-fold benefits: (i) compatibility with fracture meshing tools (e.g., PoroPy (Keilegavlen et al., 2021)), (ii) direct functionality to couple stress and (iii) geomechanics, and its open-source nature. A comprehensive description of the workflow and its application to fault networks can be found in March et al. (2020).

4. Results

4.1. Fault and fracture networks in the caprock sequences

Our study site in Konusdalen West offers a unique opportunity for detailed examination of fault and fracture networks within a regional caprock sequence. The site features caprock formations cut by low-angle normal and antithetic faults. These faults exhibit minor splays and crosscuts by other faults.

We mapped the fault and fracture network in two areas that were chosen for their representativeness of fault zone variability and the quality of the outcrop. These areas, identified in the DOM reconstruction of the main fault zone, include the central part (*Area 1*) and the portion of the fault zone just above the point where the main fault intersects a smaller fault (*Area 2*). This area is characterised by hanging-wall splays, indicative of the structural complexity in this segment of the fault zone (see Figs. 3, 4). However, our maps contain blank sections due to debris partially covering these areas, which may potentially obscure or conceal fractures see Figs. 5, 6. Consequently, some fractures might exist beneath the debris.

4.1.1. Area 1

Area 1 is situated in the lower portion of the outcrop section (Fig. 4) and encompasses the lower part of the main fault, along with at least two minor fault splays oriented $\approx 60°$ clockwise from the main fault trace (Fig. 5a). We identified a total of 505 visible fractures in this area, with lengths ranging from 0.05 to 73 m. The wide range of fracture lengths spanning three orders of magnitude allows for a robust statistical analysis (Bonnet et al., 2001). Maximum Likelihood Estimation (MLE) and Kolmogorov–Smirnov (K–S) tests were used to assess the more likely statistical distribution of fracture traces in *Area 1* (Fig. 5c). The MLE method calculates the probability of observing a fracture of a certain length or longer, based on the fitted model (power law, exponential, or lognormal). Each point on this plot represents a fracture, with the y-axis indicating the probability of finding another fracture of equal or greater length, derived from the statistical model parameters. The results indicate a 99% probability of a lognormal distribution being the more likely underlying statistic for the data, compared to 89% for exponential and 72% for power law. Moreover, the lognormal fit includes all data points, while both exponential and power law fits exclude the tails of the data. However, due to resolution limitations introduced by debris cover, we cannot rule out censoring or truncation artefacts that may affect the evaluation of the best fit (Bonnet et al., 2001).

From the colour-coded map of fracture orientations and the corresponding rose diagram (Fig. 5d-e), we distinguish a NE-SW trending normal fault and an associated conjugate set of fractures striking NW-SE. Fig. 5 also reveals the presence of a vertical, E–W striking set of fractures. This vertical set of fractures is primarily distributed in the top right-hand side of the fracture trace map (Fig. 5d), and the fracture traces appear to be confined within specific rock layer thicknesses.

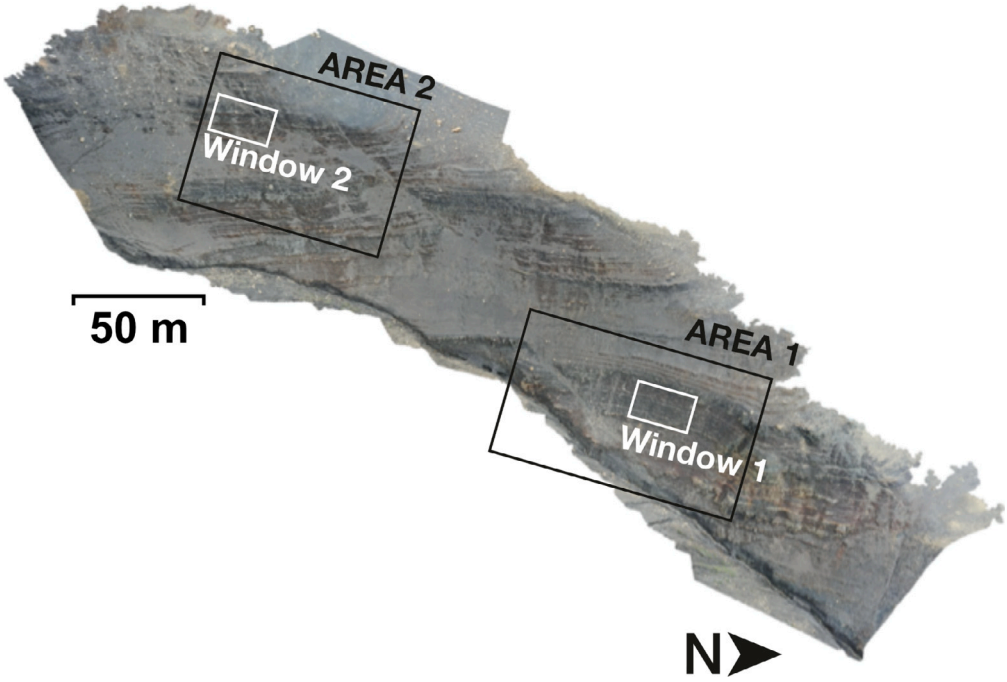

Fig. 4. South-north orthomosaic showing the whole studied vertical section in the Konusdalen West outcrop. Areas with fracture networks digitised are indicated by black rectangles; white inset areas used for permeability modelling are indicated.

4.1.2. Area 2

Area 2 is located in the top left corner of the section studied (Fig. 4). In this area, the main fault zone displays a dense array of subsidiary faults and fractures that branch off the main fault trace at an acute angle (≤ 40° clockwise). The presence of these horsetail branch faults suggests that Area 2 is at the tipping-zone of the main normal fault e.g., (Davatzes and Aydin, 2003; De Joussineau et al., 2007a; De Joussineau and Aydin, 2007b; Perrin et al., 2016). Recent work by Betlem et al. (2024), however, suggests a more complex setting, where the largest branch appears to be a crosscut, offset fault with a north–south strike. However, our ability to fully characterise the fault and fracture network is limited by debris covering the lower portion of this area (see Fig. 6a) as well by the discontinuation of the outcrop.

Despite this limitation, we identified 807 fractures in Area 2 (Fig. 6), ranging from 0.09 to 50 m in length. As in *Area 1*, the maximum measured length corresponds to the trace of the main fault, whose measure is limited by truncation (Zeeb et al., 2013). Combining information from both areas, we deduce that the fault trace cuts through at least 200 m of the studied sections. Also, in here, given the range of fracture trace lengths spanning over three orders of magnitude, we can draw accurate statistical estimations for the more likely distribution underlying the data. For *Area 2*, the combination of MLE and K–S statistics indicates a 95% probability that a power law is the more representative distribution for fracture trace length. The probabilities for exponential and lognormal distributions are lower at 90% and 66.8%, respectively. Unlike *Area 1*, where the lognormal distribution fits the entire set of fracture lengths, the tested distributions for *Area 2* only partially fit the data, either excluding the shorter or longer tails of the distribution (Fig. 6c).

The colour-coded map for fracture orientation and the respective rose diagram (Fig. 6d – e) confirm the presence of two major fracture sets: a NE-SW set corresponding to the main fault trace and its associated subsidiary splays, and a second, almost perpendicular set compatible with linkage fractures in the main fault damage zone (Kim et al., 2004).

We selected two *Windows* within the entire studied section (Fig. 4) as inputs for the stress/permeability numerical modelling. To ensure representative permeability analyses, we chose smaller windows free from debris coverage. Both selected windows have an area of 450 m^2 (15 m × 30 m; h × w) and are situated within the damage zone of the main normal fault that cuts through the entire studied section. In these sub-areas, we primarily focused our analysis on the topological arrangement of the fracture network, specifically its connectivity, as this information can be directly used to produce analytical estimates of fracture network permeability.

4.1.3. Window 1

Window 1, depicted in the lower portion of the figure, contains a total of 147 fractures spanning three orders of magnitude in length, ranging from 0.05 to 11.56 m. The three main fracture orientations observed here correspond to (i–ii) two fault-related conjugate fracture sets (inclined sets) and (iii) a prominent vertical set. The network connectivity is ensured through a combination of Y- and X-nodes, with proportions of nodes in the order of I:214; Y:143; X:170 (Fig. 7d – e). From these values and their respective ratios, we derive dimensionless parameters to quantitatively estimate the fracture network connectivity (see Appendix B for details on the equations used).

The triangular plot in Fig. 7e displays the node ratios for the fracture network in *Window 1*. The network connectivity plots on the C_L 3.57 contour, indicating good connectivity (Eq. (9) in Appendix B). Values of connection per branches (C_B), average degree ($\langle D \rangle$), and the (N_B/N_L) ratios all suggest good connectivity for the fracture network in Window 1 (Table 1). Analytical permeability estimations (Suzuki et al., 1998) yield a permeability tensor (Eq. (6)) in the flow direction, with ($k_1 = 7.6 \times 10^{-18}$ m^2); ($k_2 = 3.8 \times 10^{-18}$ m^2) with (k_1) azimuth = 17° from the vertical (Fig. 7c). In contrast, using the topological information as in the Sævik and Nixon (2017) method, we estimate a permeability of (2.0×10^{-19} m^2).

4.1.4. Window 2

Window 2 contains a total of 353 fracture traces, with lengths ranging from 0.09 m to 16.49 m. In this portion of the outcrop, we observe three main fracture sets (Fig. 8a – b): two corresponding to the fault-related conjugate sets (compare with the rose diagram for *Window 1* in Fig. 7b) and a third prominent oblique fracture set (coloured purple). The triangular plot in Fig. 8e shows that, in this portion of the

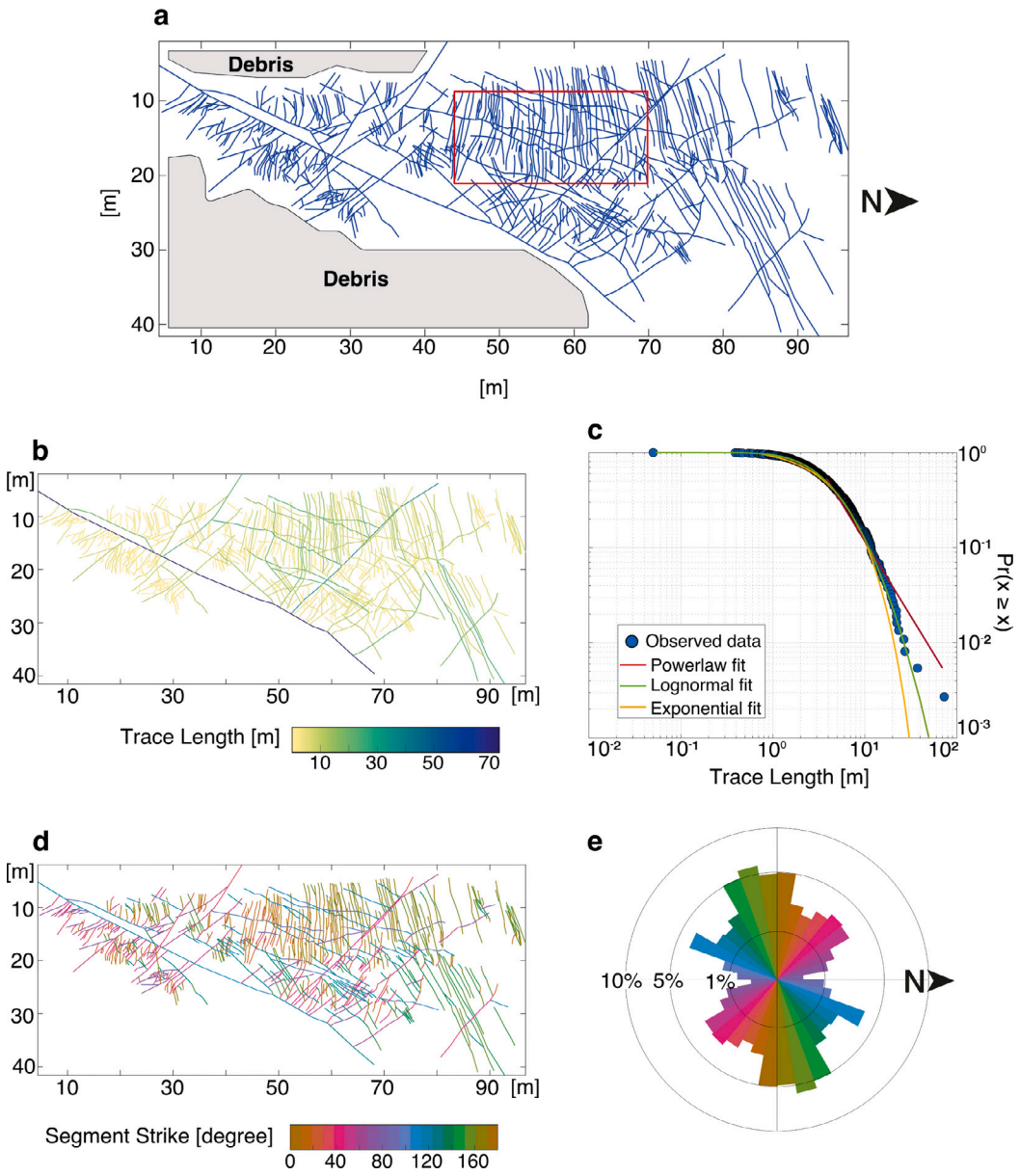

Fig. 5. Statistics for the fracture network data of *Area 1*. (a) Fracture trace map. In shaded grey are masked the area covered by debris; the red box indicates the location for *Window 1*. (b) Map of fracture traces colour-coded according to fracture length (dark colour long fractures, light colour short fracture traces). (c) Best-fitting the fracture trace length data using a Maximum-Likelihood Estimation for power law, lognormal and exponential distribution. (d) Fracture traces colour-coded by strike; 0° reference is taken from the vertical *Y*-axis. (e) Rose diagram showing fractures' strike distribution, reference 0° is the vertical (Y) axis.

fault zone, connectivity is predominantly ensured by abutments (i.e., Y-nodes); however, the network plots below the percolation threshold (corresponding to the $C_L \geq 3.57$ contour).

For *Window 2*, located higher up in the stratigraphy, connectivity parameters indicate a connected network (Table 1) but with a lower degree compared to *Window 1*. Analytical permeability estimations yield a permeability tensor in the flow direction of ($k_1 = 7.5\times10^{-18}$ m^2), ($k_2 = 4.2\times10^{-18}$ m^2), and (k_1) azimuth = 19° from the vertical (Fig. 8c). Using the topological information Eqs. (7) and (8), we estimate permeability to be (1.2×10^{-20} m^2), one order of magnitude lower than the estimated values for *Window 1*.

Table 1
Connectivity parameters for the two portions of the fault damage zone analysed (Window 1 and 2): Number of lines (N_L); Number of branches (N_B); ratio between N_B and N_L; connection per line (C_L); connection per branches (C_B); and average degree ($\langle D \rangle$). See Appendix B for definitions and formulations.

Connectivity parameters	Window 1	Window2
N_L	526	1039
N_B	661	1150
N_B/N_L	3.7	2.4
C_L	3.51	2.5
C_B	1.67	1.6
$\langle D \rangle$	2.5	2.2

4.2. Laboratory stress-permeability experiments

Using the method described in Section 3.2, we derived the parameters providing a permeability trend over the original permeability measurements for the Carmel claystone. Details on the derived parameters are given in Table 2 and shown in Fig. 9. From the parameters

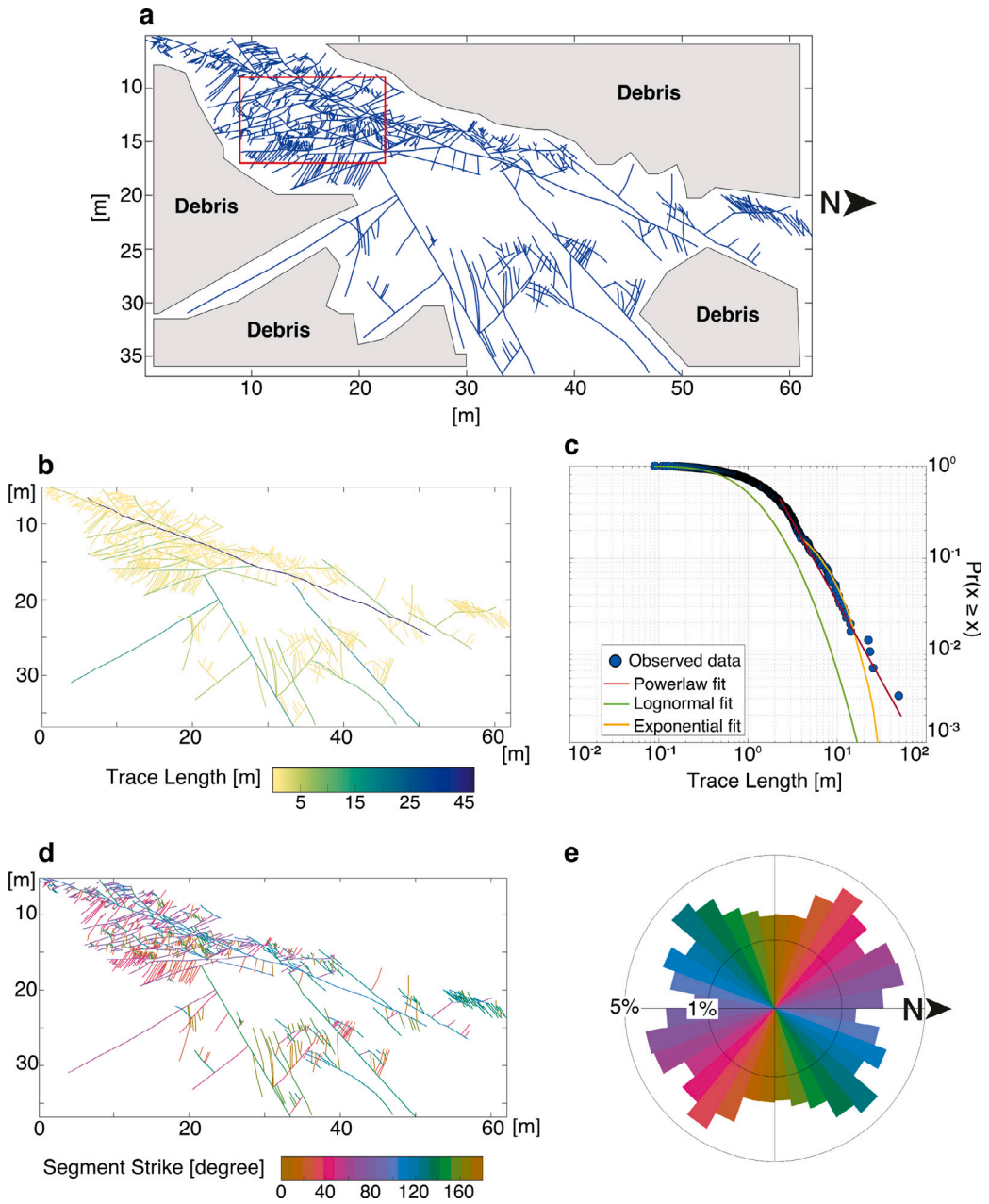

Fig. 6. Statistics for the fracture network data of *Area 2*. (a) Fracture trace map. In shaded grey are masked the area covered by debris; the red box indicates the location for *Window 2*. (b) Map of fracture traces colour-coded according to fracture length (dark colour long fractures, light colour short fracture traces). (c) Best-fitting the fracture trace length data using a Maximum-Likelihood Estimation for power law, lognormal and exponential distribution. (d) Fracture traces colour-coded by strike; 0° reference is taken from the vertical *Y*-axis. (e) Rose diagram showing fractures' strike distribution, reference 0° is the vertical (Y) axis.

derived from fitting the data (Fig. 9), we then calculate the fracture apertures for Carmel claystone over a range of effective stress conditions.

4.3. Upscaled permeability

We discretise the 2D fracture networks in *Window 1* and *Window 2* using a triangulated mesh that conforms to the fracture networks. Due to the difficulty of representing curved geometries within the mesh, we simplify the mapped fractures into linear segments using the two endpoints of each fracture. The mesh preserves the topology and connectivity of the fracture networks in both windows. Fig. 10 displays the triangulated mesh generated for *Window 1* (Fig. 10a) and *Window 2* (Fig. reffig10c) using the *FractureNetwork2d* class within the open-source package PorePy (Keilegavlen et al., 2021).

Table 2
Parameter values used to deduce the permeability trend for the Carmel mudrock sample. Values of k_{matrix} are based on data from other fine-grained mudrocks.

Parameter	Carmel claystone
d [m]	0.02547
k_{matrix} [m^2]	1×10^{-21}
b_c [m]	1×10^{7}
b_m [m]	5.1×10^{6}
α	0.1
β	0.84

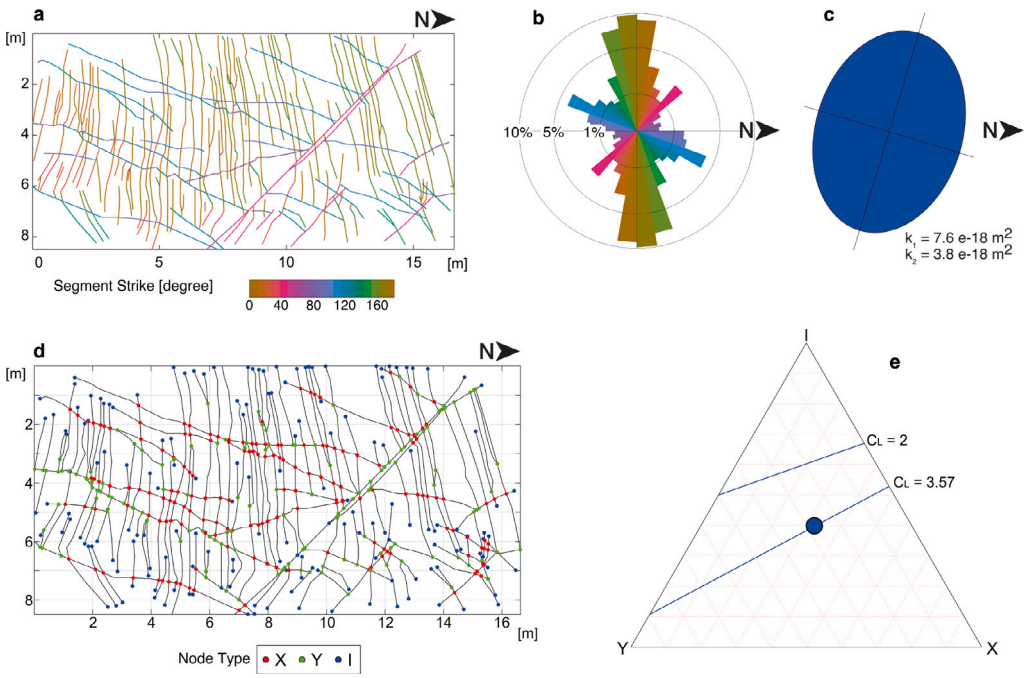

Fig. 7. Fracture network analysis for Window 1. (a) Digitised fracture network with fracture traces colour-coded by segment strike. (b) Rose diagram showing the fracture orientation distribution; 0° reference is taken from the vertical axis. (c) Permeability tensor (2D) estimated using the Suzuki's method (Suzuki et al., 1998) ($k_1 = 7.6 \times 10^{-18}$ m^2; $k_2 = 3.8 \times 10^{-18}$ m^2 with k_1 azimuth = 17° from the vertical). (d) Fracture map showing the location and the nature of the connectivity in the fracture network. (e) Triangular plot showing the overall connectivity status for the network in Window 1, showing the proportion of each type of node (P_Y :0.27; P_X:0.32; P_I:0.4).

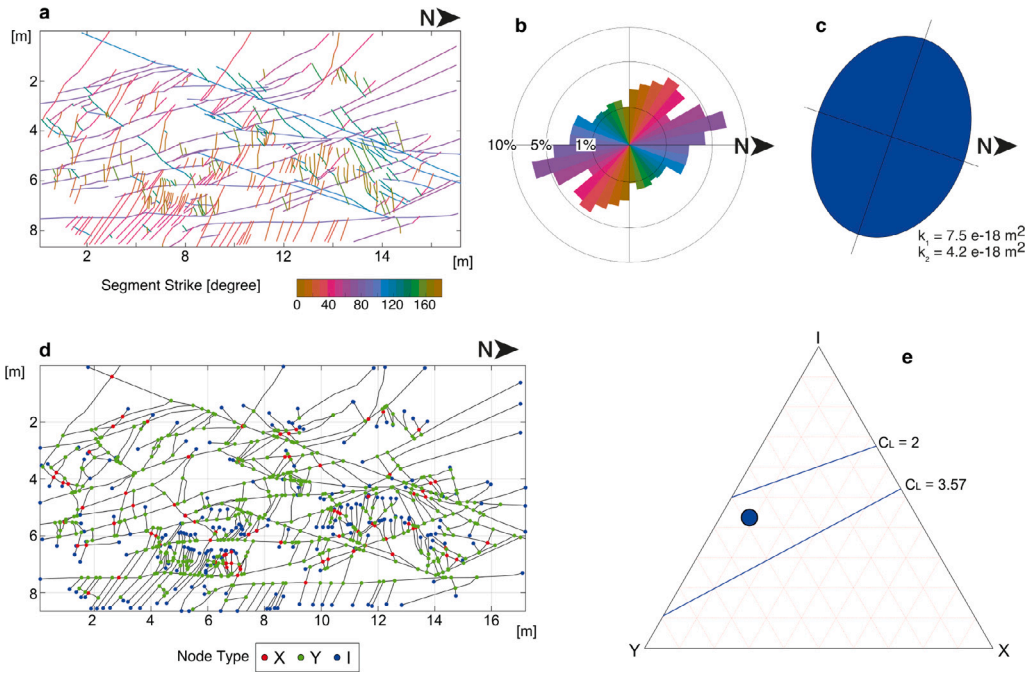

Fig. 8. Fracture network analysis for Window 2. (a) Digitised fracture network with fracture traces colour-coded by segment strike. (b) Rose diagram showing the fracture orientation distribution; 0° reference is taken from the vertical axis. (c) Permeability tensor (2D) estimated using the Suzuki's method (Suzuki et al., 1998) ($k_1 = 7.5 \times 10^{-18}$ m^2; $k_2 = 4.2 \times 10^{-18}$ m^2 with k_1 azimuth = 19° from the vertical). (d) Fracture map showing the location and the nature of the connectivity in the fracture network. (e) Triangular plot showing the overall connectivity status for the network in Window 1, showing the proportion of each type of node (P_Y :0.48; P_X:0.08; P_I:0.44). These estimates do not consider any stress variation in the network.

On the meshed fracture network, we apply stress boundary conditions ranging from 1 to 20 MPa in horizontal and vertical directions to determine the relationship between stress and fracture network permeability. We choose this range as it reflects both, the experimental data determined and the lower range of effective stresses expected in CCS projects. It is important to note that our numerical estimates of 2D fracture network permeability might be simplified compared to values in a real 3D space since the third dimension could not be directly mapped from the outcrop.

Fig. 10 displays also the upscaled permeability (in the *y*-direction) in log scale for both mapped fracture networks (*Windows 1* and *2*) under different stress conditions, considering the modelled single fracture

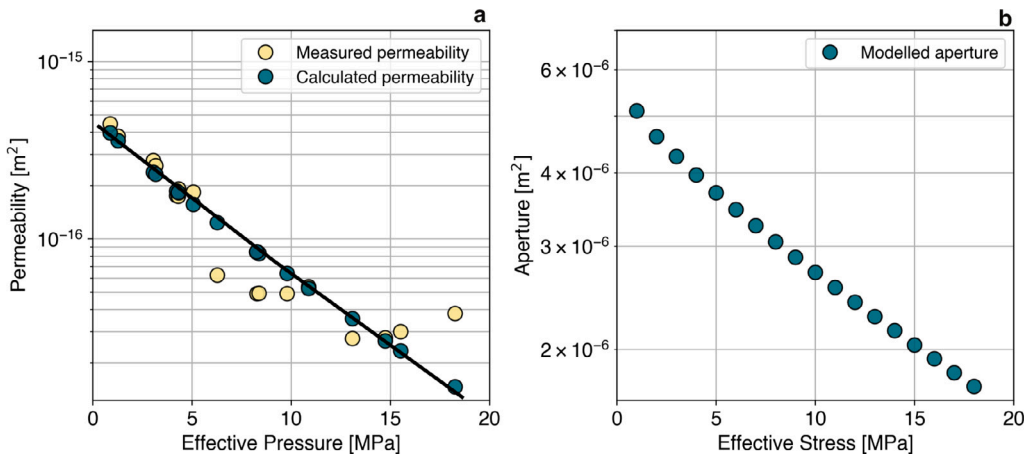

Fig. 9. (a) Measured and calculated permeability trend of the Carmel mudrock (using parameter values from Table 2). (b) Fracture aperture for the Carmel mudrock, over a range of effective stress conditions.

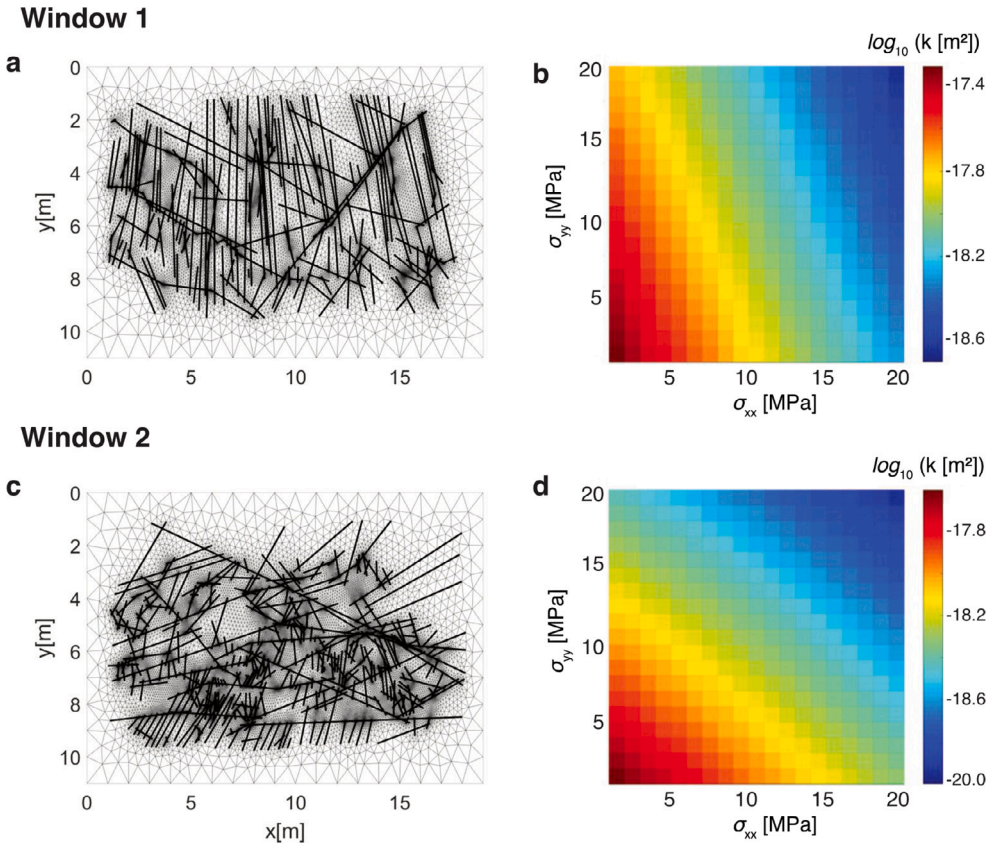

Fig. 10. Computational triangular mesh and the corresponding stress-permeability surface plots for fluid flow in *y*-direction for *Window 1* and *Window 2*. For the triangular meshes a buffer zone is considered around the fracture networks to avoid boundary effects for geomechanical computation. This buffer is only used for geomechanical computation and is removed for flow-based upscaling.

permeabilities (see Fig. 9b). The results show that upscaled fracture network permeability varies by approximately two orders of magnitude. Permeability is higher at low stresses and decreases as stress increases due to the increased normal stress on the fractures in the network. Overall, *Window 1* exhibits higher upscaled permeabilities compared to *Window 2*. In *Window 1*, we observe a clear stress direction dependency for simulated permeability: it decreases more rapidly with an increase in σ_{xx} compared to smaller slopes when the vertical stress, σ_{yy}, varies (Fig. 10b). Conversely, the upscaled permeability values in the surface plot for *Window 2* display a nearly radial distribution, likely due to a simultaneous dependency of the upscaled permeability on vertical and horizontal stresses (Fig. 10d).

5. Discussions

5.1. Fault zone fracture network

Our analysis of fracture networks reveals significant differences between the two sample windows in the fault damage zone studied within shale sequences in the Konusdalen West Valley area (Fig. 4). The most notable differences between *Area 1* (in the lower-right portion

of the fault zone) and *Area 2* (in the top-left portion of the fault) involve fracture length and orientation distributions. We interpret these differences as representative of the complex tectonic and deformation history of the Konusdalen West Valley.

Specifically, the fracture network in *Area 1* (and consequently the selected sub-area, *Window 1*) is dominated by vertical fractures, with a length distribution best described by a lognormal relationship. Following Ogata et al. (2014) we interpret these structures as a product of ENE–WSW horizontal compression linked to the WSFB, assuming that in foreland settings, the main regional joint sets are aligned parallel to the maximum regional horizontal paleostress of the associated fold-and-thrust belt. Therefore the vertical fractures formed concurrently with layer-parallel shearing responsible for the development of the normal fault. However this high-angle structures result reactivated during the Cenozoic uplift and unloading. Further development of these high-angle fractures occurred due to the uplift and unloading during the Cenozoic and glaciation and deglaciation unloading during the Quaternary (Ogata et al., 2014). Although widespread throughout the studied section, this set of vertical fractures appears more evident in *Area 1* as it cuts through coarse silty/sandy layers of the succession (Betlem et al., 2024). In contrast, *Area 2*, which is situated at the tip of the main fault zone and impacted by the cross-cutting of faults, exhibits less apparent vertical fractures. This area cuts through thin-layered shale sequences, possibly leading to the reduced visibility of fractures (Betlem et al., 2024).

Consequently, in *Area 2* (and consequently in *Window 2*), the fracture network is primarily dominated by a system of low-angle fractures (i.e., NW-SE and WNW-ESE; Fig. 11), with orientations expressed as conjugate sets to the main fault trace. These fracture sets correspond to those identified as low-angle shear fractures by Ogata et al. (2014) (there named as S1 and S2). In this of the outcrop, where with, fracture lengths are best described by a power law distribution (Fig. 6c). This suggests a development of the fracture network that is directly related to the growth of the fault, where localisation is distributed over a few long structures and associated with numerous short fractures (Cowie et al., 1995; De Joussineau and Aydin, 2007b).

The geometrical characteristics (i.e., length and orientation) and the connectivity matrix (Table 1) of the two studied areas in the fault damage zone indicate a clear link to their style and complexity. The fracture network in *Area 1* (and *Window 1*) represents a more complex system, where fault-related fractures and densely spaced vertical regional joints intersect, creating a network of percolating fractures — evidenced by a value of C_L = 3.51. On the other hand, at the fault tip (*Area 2* and *Window 2*), the network is dominated by shorter low-angle fault-related fractures, with an increased proportion of abutments (i.e. Y-nodes), but overall, with lower connectivity values (i.e. C_L = 2.5) than those measured for *Window 1*.

For *Area 1* the range in fracture orientations and the increased number of intersections helps maintain flow pathways, due to a greater probability that fractures are optimally oriented to remain open in any given stress-field (Fig. 10b). Thus, in rocks with low matrix permeability, such as the shale sequences studied here, structurally complex zones can represent highly permeable conduits for fluids to flow (e.g., Nixon et al. (2020)).

Outcrop analysis, especially for structures larger than 100 m, like the Konusdalen West faults, can help refine seismic interpretations and informs the extrapolation of these structures into the sub-surface (Howell et al., 2014). Outcrops provide a detailed examination of structural elements, including various parts of the fault zone, intersections, and splays (Ø et al., 1998; Volatili et al., 2022). However, the use of outcrops as analogues of sub-surface scenarios has inherent limitations. Their limited exposure and essentially two-dimensional perspective restrict the depth of insights they can offer for the complex, three-dimensional sub-surface environments (Shipton et al., 2002). To overcome these constraints, it is essential to integrate outcrop-derived insights with comprehensive sub-surface data. This approach respects the unique conditions and scale differences of sub-surface environments. Such integration is crucial for applying findings effectively in modelling and assessing sub-surface fault zones, particularly in CCS and hydrogen storage projects.

5.2. Control of fracture network geometry on permeability modelling and differences in analytical estimation of permeability

As previously discussed, more structurally complex networks are generally better connected. This geometrical complexity (i.e., orientation, length, connectivity) also directly impacts the simulated upscaled fracture network permeability and, consequently, flow behaviour within a fault damage zone (March et al., 2020). This is evident in the numerical simulations of upscaled permeability computed for the two selected *Windows* (Fig. 10). In *Window 1* (Fig. 10a), the long vertical fractures along the *y*-direction experience greater stresses applied from the horizontal direction than from the vertical direction. Simultaneously, these vertical fractures trend in the same direction as the flow, directly connecting the vertical flow boundaries. In contrast, shorter and more heterogeneously oriented fractures in *Window 2*, result in less anisotropic stress distribution and the radial distribution of upscaled permeability values seen in the surface plot (Fig. 10b – d). March et al. (2020) obtained similar results when analysing a fault network related to the Main Fault cutting the Opalinus Clay in the Mont Terri underground rock laboratory (Switzerland). Taking also into account the differences in connectivity between fracture networks, Manzocchi (2002) and Sanderson and Nixon (2018) argued that if a network is below the percolation threshold (i.e., $C_L \leq 3.57$), the permeability of the rock would mainly be a function of the rock matrix, but above this threshold, it would be controlled by the fracture network. In our case, the two networks lay at two different positions with respect to the percolation threshold on the I-Y-X ternary diagram, with *Window 1* very close to the limit of a fully percolating network, and *Window 2* well below it. The two studied damage zone areas therefore express different fluid flow scenarios. Here, *Window 1* represents a setting where fractures are more conductive than the matrix, thus enhancing fluid flow. In contrast, *Window 2* represents a setting where flow might be lower as fractures offer no enhancement to flow than would exist through the matrix.

The calculated permeability may be biased by an overestimation of fracture counts, as some fractures mapped on the 2D orthomosaic extracted from the 3D outcrop model may not be a direct result of faulting. Instead, they could be related to post-glacial rebound and unroofing, which have affected the study area, as well as a result of other periglacial processes. These processes might have led to decompaction and reworking of pre-existing fractures (Ogata et al., 2014; Mulrooney et al., 2018), thereby increasing their number. Despite this, the influence of fracture length, orientation, and connectivity on network permeability remains evident. These effects can be especially pronounced around fault zones, where a dense network of fractures with both high and low-angle sets can enhance flow. This observation is supported by open-hole water injection tests conducted for the pilot-scale Longyearbyen CO_2 Laboratory (Ogata et al., 2014). The calculated permeability exceeded the measured matrix permeability by approximately one order of magnitude, and the enhanced injectivity was attributed to an extensive natural fracture network (Bohloli et al., 2014; Mulrooney et al., 2018).

Numerical simulations, such as those presented here, are invaluable tools for modelling the variation in permeability related to changes in the stress states in complex fracture networks. They also help to illustrate the effects of fracture geometrical variability on fluid flow, particularly in fault zones. However, for fast appraisals, analytical methods are often used to compute equivalent fracture permeability. We here present results obtained following the methods proposed by Suzuki et al. (1998) and Sævik and Nixon (2017), respectively. Analytical methods are generally limited as they only consider average values

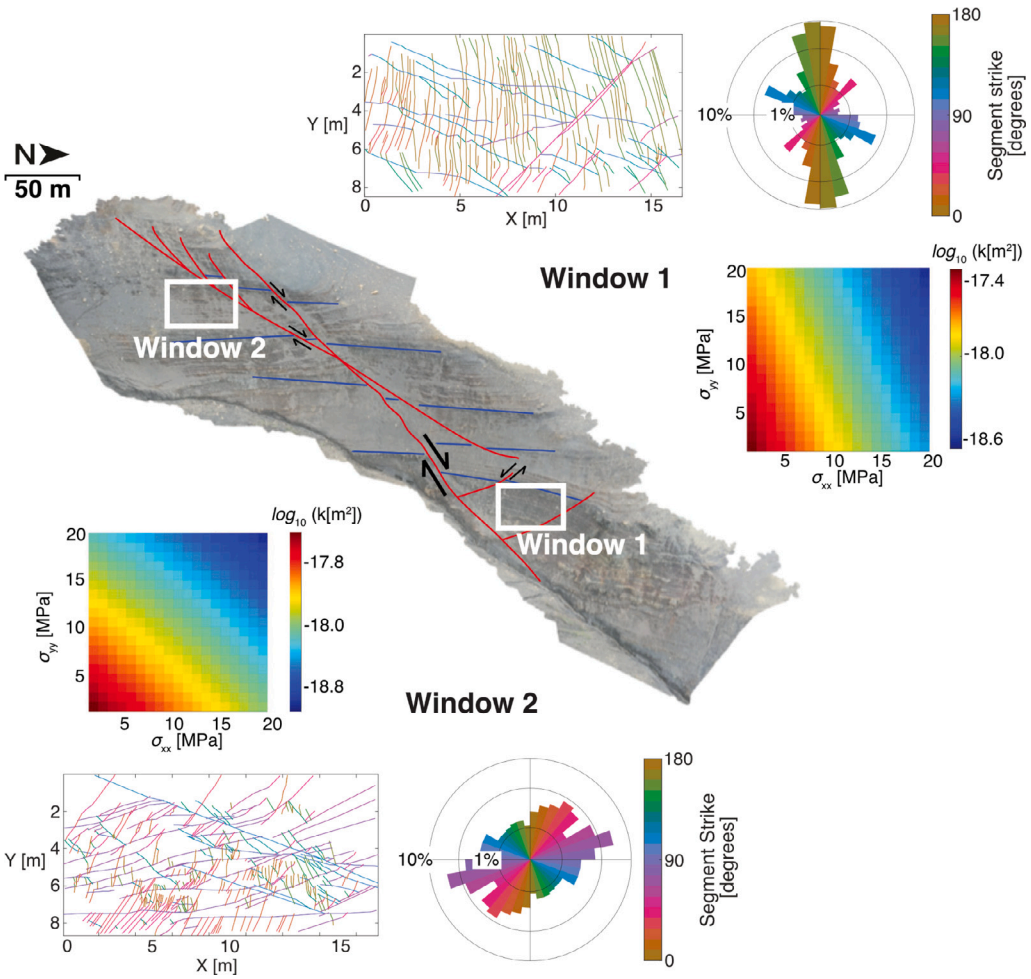

Fig. 11. Schematic showing the analysed fracture networks in relation to the main fault trace superimposed on the generated orthomosaic. Fault traces are shown as red lines, while visible sedimentary layers offset by faulting are shown as blue lines. These can be used as markers to interpret relative movement near the fault zone. The location of the fracture networks used for numerical simulation are indicated in the white squares. For both these portions (*Window 1* and *Window 2*) the fracture maps and the relative rose plots are colour-coded by trend, as well as the stress/permeability surface plots resulting from numerical simulations.

of the different parameters (such as length and aperture), thus producing "bulk" estimations of permeability. Analytical methods are also hindered by the inability of incorporating stress changes, which is important in modelling real case scenarios of fracture permeability under in-situ subsurface conditions. Nonetheless, we found that the permeability estimations obtained following the method proposed by Suzuki et al. (1998) approximate the median values of stress-permeability surface plots for the Carmel mudrock well (compare Figs. 7c and 8c with 10b and 10d). On the other hand, results obtained applying the method proposed by Sævik and Nixon (2017) strongly underestimate permeability of the studied fracture networks. Reasons for this discrepancy might be a result of the influence that I-node fractures exert on Eq. (8). If I-nodes make up a large proportion of the total nodes, Eq. (8) tends to approach small values (and can even become negative), which implies a lack of coherency in the permeability estimated (Alvarez et al., 2021).

The discrepancies observed between the results of the analytical methods and our numerical simulations highlight the limitations of the former when dealing with complex, real-world systems under varying stress conditions. While both methods contribute valuable insights to our understanding of fracture network permeability, the numerical simulation can provide better constrains to model permeability under different stress conditions. As such, the comparability of these methods may be limited, underscoring the importance of comprehensive numerical modelling in capturing the complexities of in-situ subsurface conditions.

Our numerical method, following the approach by March et al. (2020), is limited to considering normal stress versus aperture (mode 1 opening) and does not account for the impact of slip or shear deformation on fracture permeability, which falls outside the current scope. This has been investigated by some authors (e.g. Cuss et al. (2011), Krietsch et al. (2020), Kluge et al. (2021), Cappa et al. (2022)) who demonstrate that the interplay between shear displacement, aperture and consequently permeability evolution are coupled, and that shearing can cause an initial increase in permeability. An important extension to this current study would be to measure the permeability evolution of a fractured mudrock undergoing shearing to understand the fundamental mechanisms underpinning this coupled process.

In our simulations, we utilised Carmel claystone due to its mechanical similarities to the Agardhfjellet shale found in the study area. This choice was not arbitrary, but a carefully considered decision to reflect the geological reality of the site as closely as possible. Nevertheless, it is important to acknowledge that actual fracture permeability, as estimated using both analytical methods and numerical models, can be significantly influenced by the mechanical properties of the specific rock type under consideration (Snippe et al., 2022).

For this reason, while the results from our numerical modelling, based on fracture permeability data from the Carmel Formation, may not be directly applicable to the Longyearbyen CO_2 project, they highlight the criticality of employing a comprehensive approach to determine bulk permeability in fractured systems. This is particularly pertinent for complex, anisotropic fracture system associated with fault

zones. Future site specific studies should, where feasible, use data from the relevant local rock types. This study also lays the groundwork for future research using the Rurikfjellet shale, which will provide a more direct assessment of the caprock integrity for the Longyearbyen CO_2 project. Our results, therefore, extend beyond this specific case study, offering insights into the methods for evaluating permeability in fractured geological formations more generally.

Therefore, while the Carmel claystone serves as a representative model in this case, variations in rock properties could lead to different stress-permeability relationships and, consequently, different upscaled permeability models in other contexts. Future studies should therefore consider the specific rock properties of their study areas for more accurate and relevant results. An important aspect warranting further discussion is the comparison of the permeability values obtained using our approach with in-situ measurements from other geological settings. For example, permeability values reported by Ishii et al. (2011) for the Horonobe area in Japan range between 10^{-17} and 10^{-19} m^2 for Siliceous Mudstones, while permeability derived for the Main Fault within the Opalinus claystone at the Mont Terri Rock Laboratory range between 10^{-20} and 10^{-21} m^2 (Zappone et al., 2020). These ranges are consistent with the permeability values we have estimated and are within the expected range for mudstones and claystones (Shao et al., 2011). The agreement between our data and these in-situ measurements validates our methodology and reinforces its applicability across various geological settings. It is, however, essential to recognise the scale-dependency of permeability measurements and the importance of considering each study's unique geological context when interpreting such values.

5.3. Implications of fault zones for future CCS and hydrogen storage initiatives

In the broader context of future CCS projects, as well as emerging hydrogen storage initiatives, our study offers critical insights that can shape strategic decisions and operational design. Large-scale and cost-effective subsurface storage of CO_2 might increasingly include the inclusion of fault-bound structures in the future. Some examples are already being discussed, such as the Smeaheia fault block in the Norwegian North Sea (Mulrooney et al., 2020). This underscores the imperative to fully understand fault permeability, as faults can potentially act as pathways for gas leakage, whether it be CO_2 or H_2. Our integrated approach, which combines laboratory data, outcrop studies, and numerical modelling, provides a framework for evaluating fault and fracture permeability in these contexts. This framework can inform the design of containment strategies and contribute to more accurate risk assessments in CCS and hydrogen storage initiatives. Fracture network characteristics, such as length, orientation, and connectivity, can vary significantly within a fault zone, resulting in distinct flow behaviours. Furthermore, our study highlights the need for detailed fracture network information in permeability simulations. This level of detail can offer a more accurate representation of in-situ conditions, leading to more reliable predictions of potential leakage pathways in fault and fracture networks.

Given the increasing attention on fault-bound reservoirs for both CO_2 and burgeoning hydrogen storage, the application of our approach could prove particularly valuable. By elucidating the characteristics of faults in these reservoirs, we can inform the design and operation of gas storage projects, enabling more effective containment strategies, more accurate risk assessment, and ultimately, more successful storage initiatives. In addition, our findings highlight the importance of detailed fracture network information in permeability simulations. This level of detail can provide a more accurate representation of in situ conditions, leading to more reliable predictions of potential leakage pathways. As the industries of CCS (and hydrogen storage) continue to evolve and adapt, approaches like ours will be increasingly essential in ensuring the safe and effective storage of gases. We believe our study contributes significantly to this ongoing effort by providing a framework that can be used to improve our understanding of geological leakage in fault zones.

6. Summary

Seals overlying CO_2 storage formations are crucial for containment, owing to their low matrix permeability. However, the integrity of these seals can be compromised by faults and fractures, which makes understanding the characteristics of fracture networks an essential aspect of CO_2 storage site characterisation. This study introduces an integrated workflow, which combines laboratory data, outcrop studies, and numerical modelling, enabling us to quantitatively measure upscaled permeabilities in a fault damage zone, and directly apply these measurements to the assessment of fault/fracture leakage risk at CO_2 storage sites, such as the Longyearbyen CO_2 Laboratory project. We demonstrate that fracture networks within the same fault zone can exhibit significant differences. For example, we observed a percolating network formed by the coupling of a regional set of vertical joints with fault-related fractures. Conversely, a less connected network seemed to be associated with local structural complexity, and its existence did not necessarily enhance percolation. While analytical methods provide reasonable estimates of equivalent permeability for fractured systems, they may lack accuracy in analysing less connected networks. Particularly, these methods could generate misleading results for systems that fall below the percolation threshold. The analytical methods can be used as a preliminary step, providing an initial estimate of permeability within the fault and fracture networks. These methods allow us to rapidly assess the potential permeability characteristics before delving into the more complex and detailed numerical simulations. The numerical simulations then build upon these initial estimates, accounting for additional factors and complexities that are not captured in the analytical approach.

Our findings have significant implications for future carbon capture and storage (CCS) and hydrogen storage projects, especially those targeting fault-bound reservoirs. The integrated approach presented in this study can guide the design and operation of such projects, facilitating more effective containment strategies and accurate risk assessments. By identifying this structured approach, we propose a modelling strategy that balances rapid and cost-effective analytical modelling with the comprehensive insights offered by numerical hydro-mechanical simulations. This strategy optimises resource allocation and efficiency in the preliminary stages of geological appraisals, particularly in the context of CCS and hydrogen storage projects.

The comparative analysis of different methodologies in this study enhances our understanding of fracture network permeability under varied stress conditions, informing monitoring and modelling strategies in CCS. The proposed workflow can be instrumental in de-risking CCS projects by providing more reliable predictions of fluid migration through fault and fracture networks. As CCS and hydrogen storage industries continue to evolve, approaches like ours will be increasingly essential in ensuring safe and effective storage of gases. We believe our study represents a significant contribution to the ongoing efforts to ensure safe and effective storage of gases.

CRediT authorship contribution statement

Roberto Emanuele Rizzo: Conceptualization, Formal analysis, Investigation, Methodology, Software, Writing – original draft, Writing – review & editing. **Nathaniel Forbes Inskip:** Formal analysis, Investigation, Writing – original draft, Writing – review & editing. **Hossein Fazeli:** Investigation, Methodology, Writing – original draft. **Peter Betlem:** Investigation, Resources, Writing – original draft, Writing – review & editing. **Kevin Bisdom:** Investigation, Resources, Writing – review & editing. **Niko Kampman:** Conceptualization, Investigation, Resources, Writing – review & editing. **Jeroen Snippe:** Investigation, Resources, Writing – review & editing. **Kim Senger:** Methodology, Writing – review & editing. **Florian Doster:** Methodology, Validation, Writing – review & editing. **Andreas Busch:** Funding acquisition, Validation, Writing – original draft, Writing – review & editing.

Declaration of competing interest

The authors declare that they have no known competing financial interests or personal relationships that could have appeared to influence the work reported in this paper.

Data availability

The FracPaQ and the MRST MATLAB toolboxes used in this work are both freely available from the respective websites: FracPaQ and MRST. Input imagery used to reconstruct the digital model outcrop and orthomosaics are freely available from SVALBOX and the Svalbox Digital Model Database. Laboratory permeability measurement, as well as fault and fracture attribute data used to estimate analytically the permeability of the studied areas are freely available and added as Supplementary Material to this publication, as are the photogrammetry processing reports.

Acknowledgements

This project has been subsidised through the ERANET Cofund ACT, Netherlands (Project no. 271497), the European Commission, the Research Council of Norway (RCN), the Rijksdienst voor Ondernemend Nederland, the Bundesministerium för Wirtschaft und Energie, Germany, and the Department of Business, Energy & Industrial Strategy, UK. Additional support was provided by the Norwegian CCS Research Centre (NCCS; industry partners and RCN grant number 257579). We further appreciated the data provided by the University Centre in Svalbard (UNIS) CO_2 Laboratory (http://CO2-ccs.unis.no/). This work has further received funding by the European Union's Horizon 2020 research and innovation programme within the SECURe project, under grant agreement number 764531. We sincerely thank Dr. Chris Wibberley and one anonymous reviewer for their thorough and constructive comments which have greatly improved the original manuscript. We are also grateful to Dr. Diana Bacon for the editorial handling of this paper.

Appendix A. The circular scan window method for calculating fracture density

Estimates of fracture density (m^2) can be obtained using the circular scan window method of Mauldon et al. (2001). Here fracture density is estimated as $\boldsymbol{m}/2\pi^2$, where m is the number of fractures terminating within the circle of radius r. From the same approach we can also derive the estimate of fracture intensity, defined as the total length of fracture in a given area (hence units of $m/m^2=m^{-1}$), and estimated with the formula $\boldsymbol{n}/4r$, where n is the number of fractures intersecting the perimeter of the circle. In the software FracPaQ used for this work, this method is implemented by generating a 2D grid of evenly spaced circles to fit within the fracture map area. The software then calculates the intersections ($\boldsymbol{n}$) and the terminations ($\boldsymbol{m}$) of the fractures within the circles.

Appendix B. Connectivity parameters

To evaluate the degree of connectivity of a fracture network, Manzocchi (2002) and, subsequently, Sanderson and co-workers (Sanderson and Nixon, 2015, 2018; Sanderson et al., 2019) introduced a series of dimensionless connectivity parameters. These are all based on ratios between the different types of fracture intersections, such as nodes and branches. One of the main connectivity parameters that is easily determined from node counting is the average number of connections per line (C_L). This is calculated as:

$$C_L = \frac{(2N_X + N_Y)}{N_L} \tag{9}$$

where N_X and N_Y are the number of X and Y-nodes respectively, while N_L indicates the total number of lines in the analysed fracture network. For a cluster of connected lines to span a network, each line must be connected to two other lines. Thus, a network dominated by isolated nodes (I-nodes) will not be connected — and therefore unable to sustain a flow. This is indicated by values of $C_L \leq 2$. Instead, values of $C_L \geq 3.5$ are representative of fracture networks connected at the percolation threshold (Sanderson and Nixon, 2018).

Another measure describing the degree of connectivity in a fracture network is the connection per branches (C_B) parameter. The latter is calculated as follows:

$$C_B = \frac{(3N_Y + 4N_X)}{N_B} \tag{10}$$

Another parameter is the ratio between the total number of branches, N_B, and the total number of lines, N_L. These two values are calculated as $N_L = (N_I + N_Y)/2$, and $N_B = (N_I + N_Y + 4N_X)/2$. Alternatively, their ratio can be directly calculated using the proportion of X-, Y-, and I-nodes (i.e., P_X, P_Y, P_I) as following:

$$\frac{N_B}{N_L} = \frac{(4 - 3P_I - P_Y)}{(P_I + P_Y)} \tag{11}$$

A system of isolated fractures (i.e., high ratio of I-nodes) will have a $N_B/N_L = 1$, while a system of long, densely spaced, cross-cutting fractures (i.e., dominated by X-nodes) will have a $N_B/N_L \rightarrow \infty$. Instead, a network of fractures showing high proportions of Y-nodes will have $N_B/N_L \simeq 3$. Generally, natural fracture networks show values ranging between 2 (for poorly connected networks) and 10 (for fully connected systems). Lastly, the average degree ($\langle D \rangle$) is a further connectivity parameter which describes the degree to which each node is connected to branches. It is calculated as:

$$\langle D \rangle = 2\frac{N_B}{N_N} \tag{12}$$

where N_N expresses the total number of nodes in the network. When $\langle D \rangle \approx 1$ the fracture network is poorly connected, while if $\langle D \rangle \approx 4$ the network results are completely connected.

Appendix C. Supplementary data

Supplementary material related to this article can be found online at https://doi.org/10.1016/j.ijggc.2024.104105.

References

Abbas, M., 2015. Geomechanical Characterization of Shale Caprock of the Longyearbyen CO2 Storage Pilot (Master thesis).

Abu-Mahfouz, I.S., Iakusheva, R., Finkbeiner, T., Cartwright, J., Vahrenkamp, V., 2023. Rock mechanical properties of immature, organic-rich source rocks and their relationships to rock composition and lithofacies. Petroleum Geosci. 29 (1).

Aiello, I.W., 2005. Fossil seep structures of the Monterey bay region and tectonic/structural controls on fluid flow in an active transform margin. Palaeogeogr. Palaeoclimatol. Palaeoecol. 227 (1–3), 124–142.

Alvarez, L.L., Guimaraes, L.J.d.N., Gomes, I.F., Beserra, L., Pereira, L.C., de Miranda, T.S., Maciel, B., Barbosa, J.A., 2021. Impact of fracture topology on the fluid flow behaviour of naturally fractured reservoirs. Energies 14 (2021), 5488.

Amann-Hildenbrand, A., Bertier, P., Busch, A., Krooss, B.M., 2013. Experimental investigation of the sealing capacity of generic clay-rich caprocks. Int. J. Greenhouse Gas Control 19, 620–641.

Andrews, B.J., Roberts, J.J., Shipton, Z.K., Bigi, S., Tartarello, M.C., Johnson, G., 2019. How do we see fractures? Quantifying subjective bias in fracture data collection. Solid Earth 10, 487–516.

Askaripour, M., Saeidi, A., Mercier-Langevin, P., Rouleau, A., 2022. A review of relationship between texture characteristic and mechanical properties of rock. Geotechnics 2 (1), 262–296.

Betlem, P., Birchall, T., Lord, G., Oldfield, S., Nakken, L., Ogata, K., Senger, K., 2024. High resolution digital outcrop model of the faults, fractures, and stratigraphy of the agardhfjellet formation cap rock shales at konusdalen west, central spitsbergen. Earth Syst. Sci. Data 16, 985–1006.

Betlem, P., Rodes, N., Birchall, T., Dahlin, A., Smyrak-Sikora, A., Senger, K., 2023. The svalbox digital model database: a geoscientific window to the high arctic. Geosphere 19 (6), 1640–1666.

Betlem, P., Team, Svalbox, 2021. Svalbox-DOM-2019-0013-Konusdalen-West [Data Set]. Zenodo, http://dx.doi.org/10.5281/zenodo.5718376.
Birchall, T., Senger, K., Hornum, M.T., Olaussen, S., Braathen, A., 2020. Underpressure in the northern barents shelf: Causes and implications for hydrocarbon exploration. AAPG Bull. 104 (11), 2267–2295.
Bohloli, B., Skurtveit, E., Grande, L., Titlestad, G.O., Børresen, M.H., Johnsen, Ø., Braathen, A., 2014. Evaluation of reservoir and caprock integrity for the longyearbyen CO2 storage pilot based on laboratory experiments and injection tests. Norsk Geol. Tidsskrift 94, 171–187.
Bond, C.E., Wightman, R., Ringrose, P.S., 2013. The influence of fracture anisotropy on CO2 flow. Geophys. Res. Lett. 40 (7), 1284–1289.
Bonnet, E., Bour, O., Odling, N.E., Davy, P., Main, I., Cowie, P., Berkowitz, B., 2001. Scaling of fracture systems in geological media. Rev. Geophys. 39 (3), 347–383.
Braathen, A., Baelum, K., Dahl, T., Elvebakk, H., Hansen, F., Hanssen, T.H., Jochmann, M., Johansen, T.A., Johnsen, H., Larsen, L., Mertes, J., Mørk, A., Mørk, M.B., Nemec, W.J., Olaussen, S., Røed, K., Titlestad, G.O., Tveranger, J., Oye, V., 2012. Longyearbyen CO2 lab of Svalbard, Norway – first assessment of the sedimentary succession for CO2 storage. Nor. J. Geol. 92, 353–376.
Brown, S.R., Bruhn, R.L., 1998. Fluid permeability of deformable fracture networks. J. Geophys. Res. Solid Earth 103 (B2), 2489–2500.
Busch, A., Amann-Hildenbrand, A., 2013. Predicting capillarity of mudrocks. Marine Petro. Geol. 45, 208–223.
Caine, J.S., Evans, J.P., Forster, C.B., 1996. Fault zone architecture and permeability structure. Geology 24 (11), 1025–1028.
Cappa, F., Guglielmi, Y., Nussbaum, C., De Barros, L., Birkholzer, J., 2022. Fluid migration in low-permeability faults driven by decoupling of fault slip and opening. Nat. Geosci. 15 (9), 747–751.
Clauset, A., Shalizi, C.R., Newman, M.E., 2009. Power-law distributions in empirical data. SIAM Rev. 51, 661–703.
Cowie, P.A., Sornette, D., Vanneste, C., 1995. Multifractal scaling properties of a growing fault population. Geophys. J. Int. 122 (2), 457–469.
Cuss, R.J., Milodowski, A., Harrington, J.F., 2011. Fracture transmissivity as a function of normal and shear stress: First results in opalinus clay. Phys. Chem. Earth Parts A/B/C 36 (17–18), 1960–1971.
Davatzes, N.C., Aydin, A., 2003. The formation of conjugate normal fault systems in folded sandstone by sequential jointing and shearing, waterpocket monocline, utah. J. Geophys. Res. Solid Earth 108 (B10).
De Joussineau, G., Aydin, A., 2007b. The evolution of the damage zone with fault growth in sandstone and its multiscale characteristics. J. Geophys. Res. Solid Earth 112 (B2).
De Joussineau, G., Mutlu, O., Aydin, A., Pollard, D.D., 2007a. Characterization of strike-slip fault–splay relationships in sandstone. J. Struct. Geol. 29 (11), 1831–1842.
Dewhurst, D.N., Yang, Y., Aplin, A.C., 1999. Permeability and fluid flow in natural mudstones. Geol. Soc. Lond. Special Publ. 158 (1), 23–43.
Dichiarante, A.M., McCaffrey, K.J.W., Holdsworth, R.E., Bjørnarå, T.I., Dempsey, E.D., 2020. Fracture attributes scaling and connectivity in the devonian orcadian basin with implications for geologically equivalent sub-surface fractured reservoirs. Solid Earth 11, 2221–2244.
Faulkner, D.R., Mitchell, T.M., Jensen, E., Cembrano, J., 2011. Scaling of fault damage zones with displacement and the implications for fault growth processes. J. Geophys. Res. Solid Earth 116 (B5).
Gillespie, P.A., Howard, C.B., Walsh, J.J., Watterson, J., 1993. Measurement and characterisation of spatial distributions of fractures. Tectonophysics 226, 113–141.
Griffiths, L., Heap, M.J., Baud, P., Schmittbuhl, J., 2017. Quantification of microcrack characteristics and implications for stiffness and strength of granite. Int. J. Rock Mech. Min. Sci. 100, 138–150.
Healy, D., Rizzo, R.E., Cornwell, D.G., Farrell, N.J.C., Watkins, H., Timms, N.E., Smith, M., 2017. FracPaQ: A MATLAB™ toolbox for the quantification of fracture patterns. J. Struct. Geol. 95, 1–16.
Howell, J.A., Martinius, A.W., Good, T.R., 2014. The application of outcrop analogues in geological modelling: a review, present status and future outlook. Geol. Soc. Lond. Special Publ. 387 (1), 1–25.
IIPCC, 2022. Climate change 2022: Mitigation of climate change. In: Shukla, P.R., Skea, J., Slade, R., Al Khourdajie, A., van Diemen, R., McCollum, D., Pathak, M., Some, S., Vyas, P., Fradera, R., Belkacemi, M., Hasija, A., Lisboa, G., Luz, S., Malley, J. (Eds.), Contribution of Working Group III To the Sixth Assessment Report of the Intergovernmental Panel on Climate Change. Cambridge University Press, Cambridge, UK and New York, NY, USA, http://dx.doi.org/10.1017/9781009157926.
Ishii, E., Sanada, H., Funaki, H., Sugita, Y., Kurikami, H., 2011. The relationships among brittleness, deformation behavior, and transport properties in mudstones: An example from the horonobe underground research laboratory, Japan. J. Geophys. Res. Solid Earth 116 (B9).
Kampman, N., Bickle, M.J., Maskell, A., Chapman, H.J., Evans, J.P., Purser, G., Zhou, Z., Schaller, M.F., Gattacceca, J.C., Bertier, P., Chen, F., 2014. Drilling and sampling a natural CO2 reservoir: Implications for fluid flow and CO2-fluid–rock reactions during CO2 migration through the overburden. Chem. Geol. 369, 51–82.
Keilegavlen, E., Berge, R., Fumagalli, A., Starnoni, M., Stefansson, I., Varela, J., Berre, I., 2021. PorePy: an open-source software for simulation of multiphysics processes in fractured porous media. Comput. Geosci. 25, 243–265.
Kim, Y.S., Peacock, D.C., Sanderson, D.J., 2004. Fault damage zones. J. Struct. Geol. 26 (3), 503–517.
Kluge, C., Blöcher, G., Barnhoorn, A., Schmittbuhl, J., Bruhn, D., 2021. Permeability evolution during shear zone initiation in low-porosity rocks. Rock Mech. Rock Eng. 54 (10), 5221–5244.
Koevoets, M.J., Ø, Hammer, Olaussen, S., Senger, K., Smelror, M., 2018. Integrating subsurface and outcrop data of the middle jurassic to lower cretaceous agardhfjellet formation in central spitsbergen. Norsk Geol. Tidsskrift 98 (4).
Krietsch, H., Gischig, V.S., Doetsch, J., Evans, K.F., Villiger, L., Jalali, M., Valley, B., Löw, S., Amann, F., 2020. Hydromechanical processes and their influence on the stimulation affected volume: observations from a decameter-scale hydraulic stimulation project. Solid Earth 11 (5), 1699–1729.
Kubeyev, A., Forbes Inskip, N., Phillips, T., Zhang, Y., Maier, C., Bisdom, K., Busch, A., Doster, F., 2022. Digital image-based stress–permeability relationships of rough fractures using numerical contact mechanics and stokes equation. Transp. Porous Media 141 (2), 295–330.
Lie, K., 2019. An Introduction To Reservoir Simulation using MATLAB/GNU Octave: User Guide for the MATLAB Reservoir Simulation Toolbox, (MRST). Cambridge University Press, Cambridge.
Mäkel, G.H., 2007. The modelling of fractured reservoirs: constraints and potential for fracture network geometry and hydraulics analysis. Geol. Soc. Spec. Publ. London 292, 375–403.
Manzocchi, T., 2002. The connectivity of two-dimensional networks of spatially correlated fractures. Water Resour. Res. 38 (1162).
March, R., Egya, D., Maier, C., Busch, A., Doster, F., 2020. Numerical computation of stress-permeability relationships of fracture networks in a shale rock. arXiv preprint arXiv:2012.02080.
Mauldon, M., Dunne, W.M., Rohrbaugh, Jr., M.B., 2001. Circular scanlines and circular windows: new tools for characterizing the geometry of fracture traces. J. Struct. Geol 23, 247–258.
Mulrooney, M.J., Larsen, L., Van Stappen, J.F., Rismyhr, B., Senger, K., Braathen, A., Olaussen, S., Mørk, M.B.E., Ogata, K., Cnudde, V., 2018. Fluid flow properties of the wilhelmøya subgroup, a potential unconventional CO2 storage unit in central spitsbergen. Nor. J. Geol. 99, 85–116.
Mulrooney, M.J., Osmond, J.L., Skurtveit, E., Faleide, J.I., Braathen, A., 2020. Structural analysis of the smeaheia fault block, a potential CO2 storage site, northern horda platform, north sea. Mar. Pet. Geol. 121, 104598.
Niven, E.B., Deutsch, C.V., 2009. A sensitivity analysis for equivalent permeability tensors calculated from 2D discrete fracture networks. CCG Ann. Rep. 11, 1–8.
Nixon, C.W., Nœrland, K., Rotevatn, A., Dimmen, V., Sanderson, D.J., Kristensen, T.B., 2020. Connectivity and network development of carbonate-hosted fault damage zones from western malta. J. Struct. Geol. 141, 104212.
Ø, Steen, Sverdrup, E., Hanssen, T.H., 1998. Predicting the distribution of small faults in a hydrocarbon reservoir by combining outcrop, seismic and well data. Geol. Soc. Lond. Special Publ. 147 (1), 27–50.
Oda, M., 1985. Permeability tensor for discontinuous rock masses. Geotechnique 35 (4), 483–495.
Ogata, K., Senger, K., Braathen, A., Tveranger, J., Olaussen, S., 2014. Fracture systems and mesoscale structural patterns in the siliciclastic mesozoic reservoir-caprock succession of the longyearbyen CO2 lab project: Implications for geological CO2 sequestration in central spitsbergen, svalbard. Nor. J. Geol. 94, 121–154, Trondheim 2014, ISSN: 029-196X.
Ogata, K., Weert, A., Betlem, P., Birchall, T., Senger, K., 2023. Shallow and deep subsurface sediment remobilization and intrusion in the middle jurassic to lower cretaceous agardhfjellet formation (svalbard). Geosphere 19 (3), 801–822.
Olaussen, S., Grundväg, S.A., Senger, K., Anell, I., Betlem, P., Birchall, T., Braathen, A., Dallmann, W., Jochmann, M., Johannessen, E.P., Lord, G., 2024. Svalbard composite tectono-sedimentary element, barents sea. Geol. Soc. Lond. Memoirs 57 (1), M57–2021.
O'Rourke, J.E., Rey, P.H., Alviti, E., Capps, C.C., 1986. Rock index properties for geoengineering in the Paradox Basin (No. BMI/ONWI-579). Woodward-Clyde Consultants, Walnut Creek, CA (USA.
Over, J.S.R., Ritchie, A.C., Kranenburg, C.J., Brown, J.A., Buscombe, D.D., Noble, T., Sherwood, C.R., Warrick, J.A., Wernette, P.A., 2021. Processing coastal imagery with agisoft metashape professional edition, version 1.6—Structure from motion workflow documentation (no. 2021-1039). US Geological Survey.
Palladino, G., Rizzo, R.E., Zvirtes, G., Grippa, A., Philipp, R.P., Healy, D., Alsop, G.I., 2020. Multiple episodes of sand injection leading to accumulation and leakage of hydrocarbons along the san andreas/san gregorio fault system, california. Mar. Pet. Geol. 118, 104431.
Perrin, C., Manighetti, I., Gaudemer, Y., 2016. Off-fault tip splay networks: A genetic and generic property of faults indicative of their long-term propagation. C. R. Geosci. (ISSN: 1631-0713) 348 (1), 52–60.
Phillips, T., Kampman, N., Bisdom, K., Inskip, N.D.F., den Hartog, S.A., Cnudde, V., Busch, A., 2020. Controls on the intrinsic flow properties of mudrock fractures: A review of their importance in subsurface storage. Earth-Sci. Rev. 211, 103390.
Rizzo, R.E., Healy, D., De Siena, L., 2017. Benefits of maximum likelihood estimators for fracture attribute analysis: Implications for permeability and up-scaling. J. Struct. Geol. 95, 17–31.

Rizzo, R.E., Healy, D., Heap, M.J., Farrell, N.J., 2018. Detecting the onset of strain localization using two-dimensional wavelet analysis on sandstone deformed at different effective pressures. J. Geophys. Res. Solid Earth 123 (12), 10–460.

Rohrbaugh, Jr., M.B., Dunne, W.M., Mauldon, M., 2002. Estimating fracture trace intensity, density, and mean length using circular scan lines and windows. AAPG Bull. 86, 2089–2104.

Rybacki, E., Reinicke, A., Meier, T., Makasi, M., Dresen, G., 2015. What controls the mechanical properties of shale rocks? - part I: Strength and Young's modulus. J. Pet. Sci. Eng. 135, 702–722.

Sævik, P.N., Nixon, C.W., 2017. Inclusion of topological measurements into analytic estimates of effective permeability in fractured media. Water Resour. Res. 53 (11), 9424–9443.

Sanderson, D.J., Nixon, C.W., 2015. The use of topology in fracture network characterization. J. Struct. Geol. 72, 55–66.

Sanderson, D.J., Nixon, C.W., 2018. Topology, connectivity and percolation in fracture networks. J. Struct. Geol. 115, 167–177.

Sanderson, D.J., Peacock, D.C., Nixon, C.W., Rotevatn, A., 2019. Graph theory and the analysis of fracture networks. J. Struct. Geol. 125, 155–165.

Senger, K., Tveranger, J., Braathen, A., Olaussen, S., Ogata, K., Larsen, L., 2015. CO 2 storage resource estimates in unconventional reservoirs: insights from a pilot-sized storage site in Svalbard, Arctic Norway. Environ. Earth Sci. 73, 3987–4009.

Shao, H., Sönnke, J., Morel, J., Krug, S., 2011. In situ determination of anisotropic permeability of clay. Phys. Chem. Earth Parts A/B/C 36 (17–18), 1688–1692.

Shipton, Z.K., Evans, J.P., Robeson, K.R., Forster, C.B., Snelgrove, S., 2002. Structural heterogeneity and permeability in faulted eolian sandstone: Implications for subsurface modeling of faults. AAPG Bull. 86 (5), 863–883.

Snippe, J., Kampman, N., Bisdom, K., Tambach, T., March, R., Maier, C., Phillips, T., Inskip, N.F., Doster, F., Busch, A., 2022. Modelling of long-term along-fault flow of CO2 from a natural reservoir. Int. J. Greenhouse Gas Control 118, 103666.

Suzuki, K., Oda, M., Yamazaki, M., Kuwahara, T., 1998. Permeability changes in granite with crack growth during immersion in hot water. Int. J. Rock Mech. Min. Sci. 35 (7), 907–921.

van Noort, R., Yarushina, V., 2018. Water, CO_2 and argon permeabilities of intact and fractured shale cores under stress. Rock Mech. Rock Eng. 52 (2), 299–319.

Van Stappen, J., De Kock, T., Boone, M., Olaussen, S., Cnudde, V., 2014. Pore-scale characterization and modelling of CO2 flow in tight sandstones using X-ray micro-CT; knorringfjellet formation of the longyearbyen CO2 lab, svalbard. Nor. J. Geol. 94 (2–3), 201–215.

Van Stappen, J.F., Meftah, R., Boone, M.A., Bultreys, T., De Kock, T., Blykers, B.K., Senger, K., Olaussen, S., Cnudde, V., 2018. In situ triaxial testing to determine fracture permeability and aperture distribution for CO2 sequestration in Svalbard, Norway. Environ. Sci. Technol. 52 (8), 4546–4554.

Vermilye, J.M., Scholz, C.H., 1995. Relation between vein length and aperture. J. Struct. Geol. 17 (3), 423–434.

Volatili, T., Agosta, F., Cardozo, N., Zambrano, M., Lecomte, I., Tondi, E., 2022. Outcrop-scale fracture analysis and seismic modelling of a basin-bounding normal fault in platform carbonates, central Italy. J. Struct. Geol. 155, 104515.

Weismuller, C., Prabhakaran, R., Passchier, M., Urai, J.L., Bertotti, G., Reicherter, K., 2020. Mapping the fracture network in the lilstock pavement, bristol channel, UK: manual versus automatic. Solid Earth 11, 1773–1802.

Zappone, A., Rinaldi, A.P., Grab, M., Wenning, Q., Roques, C., Madonna, C., Obermann, A., Bernasconi, S.M., Soom, F., Cook, P., Guglielmi, Y., 2020. Fault sealing and caprock integrity for CO 2 storage: an in-situ injection experiment. Solid Earth Discuss. 2020, 1–51.

Zeeb, C., Gomez-Rivas, E., Bons, P.D., Blum, P., 2013. Evaluation of sampling methods for fracture network characterization using outcrops. AAPG Bull. 97, 1545–1566.

Zhang, C.L., 2011. Experimental evidence for self-sealing of fractures in claystone. Phys. Chem. Earth Parts A/B/C 36 (17–18), 1972–1980.

Zhang, C.L., 2013. Sealing of fractures in claystones. J. Rock Mech. Geotech. Eng. 5, 214–220.